Charge-symmetry breaking in *np* elastic scattering at 477 MeV

R. Abegg,[a] D. Bandyopadhyay,[b] J. Birchall,[b] E. B. Cairns,[c] G. H. Coombes,[c] C. A. Davis,[a,b] N. E. Davison,[b] P. P. J. Delheij,[a] P. W. Green,[a] L. G. Greeniaus,[a,c] H. P. Gubler,[b,*] D. C. Healey,[a] C. Lapointe,[a,†] W. P. Lee,[b,‡] W. J. McDonald,[c] C. A. Miller,[a] G. A. Moss,[c,§] G. R. Plattner,[d] P. R. Poffenberger,[b,**] W. D. Ramsay,[b] G. Roy,[c] J. Soukup,[c] J. P. Svenne,[b] R. R. Tkachuk,[c,††] W. T. H. van Oers,[b] G. D. Wait,[a] and Y. P. Zhang[b,‡‡]

[a]*TRIUMF, 4004 Wesbrook Mall, Vancouver, British Columbia, Canada V6T 2A3*

[b]*University of Manitoba, Department of Physics, Winnipeg, Manitoba, Canada R3T 2N2*

[c]*University of Alberta, Department of Physics, Edmonton, Alberta, Canada T6G 2N5*

[d]*Institüt für Physik, Universität Basel, CH-4056 Basel, Switzerland*

(Received 29 June 1988)

The effect of isospin-violating, charge-symmetry-breaking (CSB) terms in the *np* interaction has been observed at TRIUMF by measuring the difference in the zero-crossing angles of the neutron and proton analyzing powers, A_n and A_p, at a neutron energy of 477 MeV. The scattering asymmetries were measured with a neutron beam incident on a polarizable proton target. To reduce systematic errors, interleaved measurements of A_n and A_p were made using the same beam and target (apart from their respective polarization states). Neutrons and protons were detected in coincidence in the center-of-mass angle range from 59°–80°. The difference in zero-crossing angles was $0.340°\pm0.162°$ ($\pm0.058°$), which yields $\Delta A \equiv A_n - A_p = 0.0047\pm0.0022$ (±0.0008) using $dA/d\theta_{\text{c.m.}} = -0.013\,82\ \text{deg}^{-1}$. The second errors represent systematic effects. This result is in good agreement with recent theoretical calculations which include CSB effects due to the *np* mass difference in π, ρ, and 2π exchange, electromagnetic coupling of the neutron anomalous magnetic moment to the proton current, ρ-ω-meson mixing, and short- and medium-range effects of the up- and down-quark mass difference.

I. INTRODUCTION

Understanding the symmetries of a system can be a valuable guide to the construction of a theory and the simplifications necessary to make it tractable. In the study of the nucleon-nucleon (*NN*) interaction the symmetry constraints of angular momentum conservation, parity conservation, and time-reversal invariance are routinely invoked. Knowing how these and other symmetries are broken can give insight into the details of the interaction at short distances. This may be particularly true in forming the bridge between quantum chromodynamics and the effective *NN* interaction represented by one-boson exchange.

Isospin was the first internal symmetry postulated for the *NN* force.[1] The very small neutron-proton (*np*) mass difference suggested that the neutron and proton could be viewed as two states of the same particle (the nucleon) provided that the electromagnetic interaction could be turned off. By analogy with spin in ordinary space, the nucleon could have "isospin" **T** oriented up or down in "isospin space." The third component of isospin is related to the charge; conventionally the proton has $T_3 = +\frac{1}{2}$ and the neutron has $T_3 = -\frac{1}{2}$. For an interaction to be isospin invariant (or charge independent), the Hamiltonian H must be invariant under *arbitrary* rotations in isospin space,

$$[H,\mathbf{I}]=0\ , \tag{1}$$

where **I** is the isospin of the system. For the *NN* case with $\mathbf{I}=\mathbf{T}(1)+\mathbf{T}(2)$, the *nn*, *pp*, and *np* forces must be identical.

Since electromagnetic interactions break charge independence, violations on the order of the fine-structure constant are to be expected. Charge symmetry is a less restrictive constraint than isospin invariance. It only requires that H be invariant for 180° rotations about the 2 axis in isospin space,

$$[H,P_{\text{CS}}]=0,\quad P_{\text{CS}}=e^{i\pi I_2}\ . \tag{2}$$

A charge-independent interaction must also be charge symmetric, but the converse is not necessarily true. The charge-symmetry operator reverses the sign of I_3, for example, changing neutrons into protons, or π^+ into π^- and vice versa. For the *NN* system the *nn* and *pp* forces should be identical, but there is no relation between them and the *np* force. Charge symmetry also requires that isospin be conserved, so that for the *np* system there is no mixing between the $I=0$ and $I=1$ states.

Evidence for charge dependence in the *NN* interaction, after electromagnetic contributions are subtracted, is seen in the difference between the low-energy nucleon-nucleon singlet scattering lengths a_{np} and a_{pp}, and the effective ranges r_{np} and r_{pp} (Ref. 2). Charge-symmetry breaking (CSB) has been observed in the binding-energy differences of mirror nuclei, the Nolen-Schiffer effect.[3,4] The observed ^{3}H-^{3}He binding-energy difference is 764 keV. After correction for direct electromagnetic contributions,

80±24 keV of this effect remains.[5] This is consistent with the strong-interaction part of the *nn* interaction being slightly more attractive than the *pp* interaction. For heavier nuclei, the complications of the nuclear many-body problem make it very difficult to interpret the Nolen-Schiffer effect in terms of CSB components of the *NN* interaction. Comparing the singlet scattering lengths a_{nn} and a_{pp} (corrected for electromagnetic effects), the *nn* interaction again appears to be slightly more attractive than the *pp* interaction. However, the corrections for the electromagnetic effects have non-negligible theoretical uncertainties,[6,7] off-shell ambiguities in the Coulomb corrections being the worst problem. The CSB effects observed in $\pi^{\pm}d$ total-cross-section measurements[8] can be interpreted in terms of the mass differences of the various charge states of the Δ resonance. The same mechanisms are used to describe possible CSB effects observed in $\pi^{\pm}d$ elastic scattering.[9–11] Unfortunately, interpretation of these data still presents some theoretical difficulty and the results cannot be directly applied to CSB studies of the free *NN* interaction.

Henley and Miller[12] have classified the terms of the nucleon-nucleon interaction according to their isospin behavior. Class (I) forces are isoscalar in nature and conserve both charge independence and charge symmetry. Class (II) isotensor forces break charge independence but preserve charge symmetry. Class (III) isovector forces depend on $[T_3(1)+T_3(2)]$ and break both charge independence and charge symmetry but do not change the total isospin. Class (IV) forces, the class of interest here, preserve neither charge symmetry nor charge independence nor isospin, and since isospin is not conserved there is mixing of the $I=0$ and $I=1$ states of the *np* system.

There are several important reasons for measuring isospin related symmetries. In an optimistic case it is possible that an effect proportional to the up-down-quark mass difference might be found at a scale of $(m_d-m_u)/(m_d+m_u)$. More realistically, one aims to test competing conventional models of baryons interacting through meson exchange. Charge-symmetry breaking probes an untested aspect of existing theories. In particular, CSB contributions from one-boson exchange are sensitive to the low partial waves and therefore depend on the details of the short-range behavior of the *NN* potential. The description of CSB may require an explicit quark-level characterization of the short-distance strong interaction, where conventional nuclear theory breaks down.

Lorentz invariance, parity conservation, time-reversal invariance, and isospin conservation reduce from 16 to 5 the number of possible *NN* amplitudes for each value of the isospin. If L is the relative orbital angular momentum of two nucleons, S their total spin, I the total isospin, and J the total angular momentum, then the generalized Pauli principle imposes

$$(-1)^{L+S+I}=-1 \ .$$

If parity and isospin are conserved, then the total spin S is also conserved and there are no allowed spin-singlet-triplet transitions. For identical nucleons (*pp* and *nn*), the total spin is always conserved. If isospin is not conserved spin-singlet-triplet transitions are allowed for the *np* system and a sixth amplitude is needed. The scattering matrix between initial c.m. momentum $\mathbf{k}_i$ and final momentum $\mathbf{k}_f$ is given by[13]

$$\begin{aligned} M(\mathbf{k}_i,\mathbf{k}_f)=\tfrac{1}{2}[&(a+b)+(a-b)(\boldsymbol{\sigma}_1\cdot\mathbf{n})(\boldsymbol{\sigma}_2\cdot\mathbf{n}) \\ &+(c+d)(\boldsymbol{\sigma}_1\cdot\mathbf{l})(\boldsymbol{\sigma}_2\cdot\mathbf{l}) \\ &+(c-d)(\boldsymbol{\sigma}_1\cdot\mathbf{m})(\boldsymbol{\sigma}_2\cdot\mathbf{m}) \\ &+e(\boldsymbol{\sigma}_1+\boldsymbol{\sigma}_2)\cdot\mathbf{n}+f(\boldsymbol{\sigma}_1-\boldsymbol{\sigma}_2)\cdot\mathbf{n}] \ . \end{aligned} \tag{3}$$

The six complex amplitudes are a, b, c, d, e, and f, and

$$\mathbf{l}=\frac{\mathbf{k}_f+\mathbf{k}_i}{|\mathbf{k}_f+\mathbf{k}_i|}, \quad \mathbf{m}=\frac{\mathbf{k}_f-\mathbf{k}_i}{|\mathbf{k}_f-\mathbf{k}_i|}, \quad \mathbf{n}=\frac{\mathbf{k}_i\times\mathbf{k}_f}{|\mathbf{k}_i\times\mathbf{k}_f|} \ . \tag{4}$$

The CSB amplitude f can be expressed in terms of the nuclear bar phase shifts $\bar{\delta}_J$ and $\bar{\delta}_{JJ}$ (the singlet and uncoupled triplet phase shifts, respectively), and new parameters $\bar{\gamma}_J$ which are the mixing angles for the singlet-triplet transitions[14,15]

$$f(\theta)=\frac{i}{2k}\sum_{J=1}^{\infty}(2J+1)\sin 2\bar{\gamma}_J\exp(i\bar{\delta}_J+i\bar{\delta}_{JJ})d^J_{10}(\theta) \ . \tag{5}$$

The $d^J_{10}(\theta)$ represent Wigner functions.

Effects due to one-photon exchange, ρ-ω-meson mixing, and the *n*-*p* mass difference in one-boson exchange have been extensively examined in a conventional meson theoretical framework.[14–21] In the *NN* system CSB effects are small, the singlet phase shifts $\bar{\delta}_J$, and the uncoupled triplet phase shifts $\bar{\delta}_{JJ}$ can be taken directly from phase-shift analyses and the substitution $\sin 2\bar{\gamma}_J\approx 2\bar{\gamma}_J$ can be made. The $\bar{\gamma}_J$ parameters can be described[14–16] in terms of radial integrals of functions arising from various CSB mechanisms.

Only two experimental measurements appear feasible given the size of the effects to be observed:

$$2\frac{d\sigma}{d\Omega}(A_{00n0}-A_{000n})=\mathrm{Re}\,b^*f \ , \tag{6}$$

$$2\frac{d\sigma}{d\Omega}(A_{00sk}-A_{00ks})=\mathrm{Re}\,c^*f \ . \tag{7}$$

Here a four-subscript notation A_{srbt} is used to denote the polarization states of the scattered, recoil, beam, and target particles, respectively. In Eqs. (6) and (7) the index k refers to polarization along the beam direction, s is transverse to the beam direction in the scattering plane, and n is normal to scattering plane.

An investigation of the effects of CSB, isospin-mixing interactions in the *np* elastic scattering system has been carried out at TRIUMF.[22–28] The experiment is the first direct measurement of class (IV) forces. The difference between the neutron and proton analyzing powers, $\Delta A\equiv A_{00n0}-A_{000n}\equiv A_n-A_p$, was determined at the angle θ_0 where the average analyzing power crosses zero. For A_n, the scattering asymmetry was measured using 477-MeV polarized neutrons incident on an unpolarized

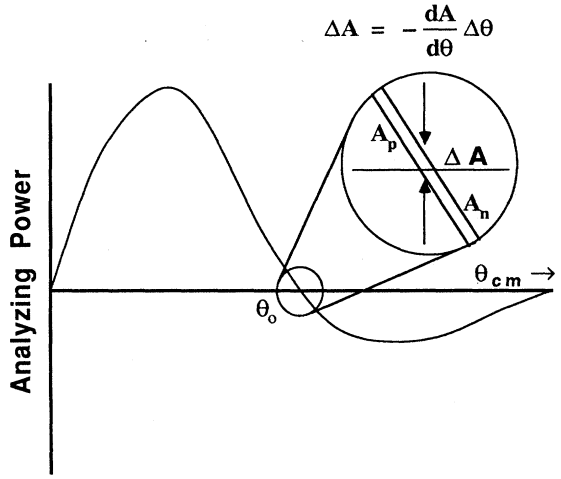

FIG. 1. An illustration of the method employed to extract $\Delta A = A_n - A_p$ from the difference in the A_n and A_p zero-crossing angles for *np* elastic scattering. $dA/d\theta$ is determined from phase-shift analyses; $\Delta\theta$ is determined in the experiment.

hydrogen target. For A_p, the polarization states of the beam and target were interchanged. The value of ΔA at the zero crossing was determined indirectly from the difference between the zero-crossing angles of the separate analyzing-power angular distributions. The principle of the measurement is shown schematically in Fig. 1. Phase-shift predictions of $dA/d\theta$ were used to relate the experimentally observed angle difference to ΔA. The choice of an angle range including θ_0 was made to reduce systematic errors to a minimum. In particular, the A_n and A_p zero-crossing angles are independent of the beam and target polarizations. In any direct absolute measurement of ΔA, uncertainties in these latter parameters can dominate the expected CSB effect.

The experiment was done using left-right-symmetric pairs of detection telescopes[23] to observe in coincidence the scattered and recoil particles from *np* elastic scattering. The same equipment and detector configuration were used to measure both A_n and A_p. The determination of the angle difference is then a null measurement where systematic errors common to both measurements cancel. The A_n and A_p measurements were interleaved to eliminate the effects of long-term instabilities in the detection equipment and beam properties. Use of apparatus symmetric about the neutron beam direction, and elimination of geometric changes between the A_n and A_p phases of the experiment resulted in the cancellation of most geometric systematic errors in ΔA to at least first order. Further systematic errors not correlated with beam or target polarization reversal were canceled to at least first order by frequently reversing the neutron and proton polarizations. Since the difference in the zero-crossing angles, $\Delta\theta$, does not depend on the beam or target polarizations nor on the actual values of the scattering angles, absolute angle measurements were not required. However, all angular parameters were determined as accurately as possible to reduce possible systematic effects and to allow consistency checks to be made. In this experiment $A_n(\theta)$ and $A_p(\theta)$ were not measured absolutely since $\Delta\theta$ can be determined directly from the zero crossings of the scattering asymmetries.

The polarized-neutron-beam facility,[22] the detection equipment,[23] and the frozen spin target (FST) (Refs. 24–26) have been discussed in detail in earlier papers and are summarized only briefly in Sec. II. Section III contains a summary of the techniques used in the data analysis: the extraction of ΔA from the data and the evaluation of the contribution of the background asymmetry to the result. In the conclusion, the results are summarized along with a discussion of the experimental systematic error.

The values presented here differ by about one-half of a standard deviation from our earlier publication.[27] They represent the results of a more extensive analysis of the experimental data and supersede the earlier results. Part of the difference from the earlier result for ΔA stems from the use of a more recent prediction for the slope parameter $dA/d\theta_{\text{c.m.}}$. More detail concerning the experiment is contained in a thesis.[28]

II. EXPERIMENTAL DETAILS

A schematic diagram of the proton-beam transport, and the neutron-beam production system and the apparatus is given in Fig. 2. The neutron beam was created via the $^2\text{H}(\vec{p},\vec{n})2p$ reaction. Right-handed coordinate

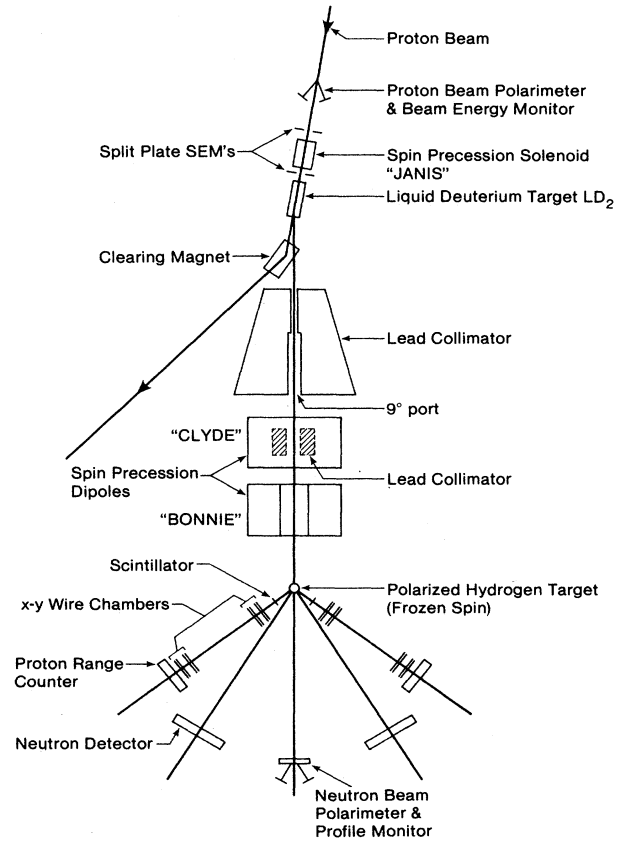

FIG. 2. Details of the proton-beam transport system and experimental apparatus. The figure is not to scale.

systems are used with z along the incident proton direction, y vertically up, and x horizontal. Primes will be used to denote the final-state neutron system. The experiment required that the proton beam be stable in energy, position, and direction at the liquid-deuterium (LD_2) neutron production target.

A. Primary proton beam

To maintain a consistent position on the LD_2 target, the x and y positions of the primary proton beam were monitored with two split-plate secondary-emission monitors (SEM's) situated 0.86 and 2.18 m upstream of the LD_2 target. Each SEM consisted of five parallel, 8-μm-thick aluminum foils. The second and fourth foils were split into left-right and up-down electrically isolated halves (1-mm gap), respectively, so that each SEM gave both x and y position information. SEM output signals were read every 5 sec by a microprocessor system programmed to calculate left-right and up-down current asymmetries and apply appropriate beamline element corrections. Changes in the SEM asymmetries were directly correlated to the variation of the proton beam position. The feedback system employed a bending magnet, a horizontal steering magnet, and two vertical steering magnets.

Left-right and up-down SEM beam-current asymmetries observed during a typical 2-h run are shown in Fig. 3. Based on beam profile monitor information, the size of the proton-beam spot was about 5 mm full width at half maximum (FWHM) wide and 4 mm FWHM high near the LD_2 target. Assuming a Gaussian beam shape, the position and angular uncertainties of the primary beam at the LD_2 target were conservatively estimated to be $\sigma_x < 0.15$ mm, $\sigma_y < 0.15$ mm, $\sigma_{\theta x} < 0.006°$, and $\sigma_{\theta y} < 0.004°$. No unacceptable SEM asymmetries were recorded. The beam position stability was sufficiently good that the influence of beam motion on systematic errors in ΔA is $< 10^{-4}$. No significant differences in the mean proton-beam position for different beam polarization states were observed.

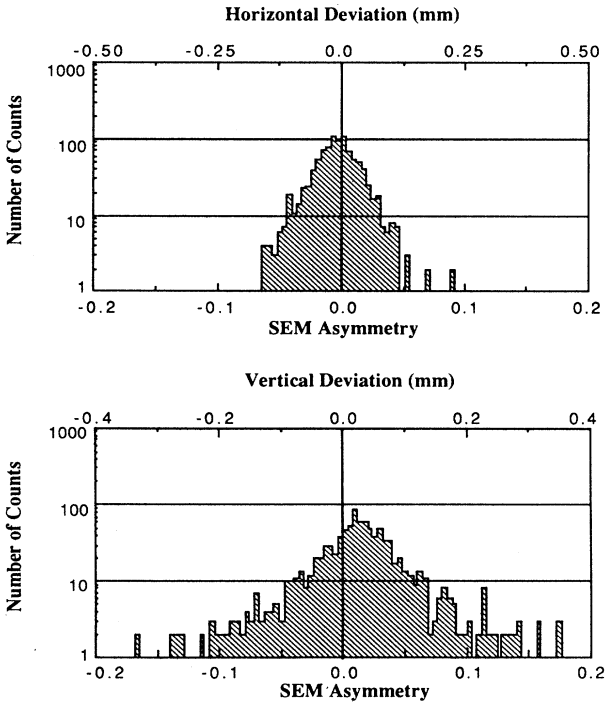

FIG. 3. Horizontal and vertical current asymmetry distributions from the split-plate secondary emission monitors (SEM's), illustrating the stability of the primary proton beam. The dependence of the asymmetry on position is almost linear. The estimated beam centroid displacements are shown at the top of the plots.

The polarization was cycled between up, down, and unpolarized states at the ion source. It was not necessary to determine the actual proton-beam polarization. However, it was measured with reasonable precision to help maintain as high a polarization as possible and to allow monitoring of other possible systematic errors. The proton polarimeter (see Fig. 2) was located in a large scattering chamber. Protons scattered at 17° in the laboratory were detected in coincidence with the conjugate recoil particles observed in scintillator detectors at $\pm 68.9°$. Left-right scattering asymmetries (corrected for accidental coincidences) were calculated from scalers for all polarization states every 5 min for monitoring purposes and later averaged for every 2-h data run. Unpolarized beam was used to monitor instrumental asymmetries. Left-right scattering asymmetries were corrected for the polarimeter instrumental asymmetry and for the effect of observed pp pairs from $(p,2p)$ reactions on nonhydrogenous components in the target. The instrumental asymmetry was -0.018 ± 0.002 and remained stable throughout the duration of the experiment. The observed asymmetries were increased by a factor of about 1.03 to account for $(p,2p)$ reactions. The average proton polarization was 0.65 and ranged from a low of about 0.6 to a high of about 0.7. The y polarization component of the incident proton beam was precessed by 90° with a superconducting solenoid into the x direction for production of the neutron beam.

The experiment was designed so that an absolute calibration of the primary proton-beam energy was not required. However, it was necessary to maintain a constant proton-beam energy because of the energy dependence of the np zero-crossing angle;[29,30] $d\theta_0/dE_n \approx 0.018°/\text{MeV}$ (in the c.m.) at 477 MeV. Variation of the mean proton energy by 0.5 MeV between measurements of A_n and A_p affects ΔA at the 10^{-4} level. The proton energy stability was monitored with a beam-energy monitor[31] (BEM) which consisted of range counter assemblies at $\pm 17.0°$ relative to the beam axis after the forward detectors of the proton polarimeter. Each range counter assembly consisted of six 1-cm-thick scintillators separated by 1-mm-thick copper absorbers preceded by a copper degrader. The BEM observed a fraction of events which triggered the polarimeter and the degrader was chosen so that the pp elastic protons stopped in the middle of the scintillator stack. The mean proton-beam energy in each range assembly was determined from the numbers of protons which stopped between each of the counters. The left- and right-energy values were averaged to reduce ki-

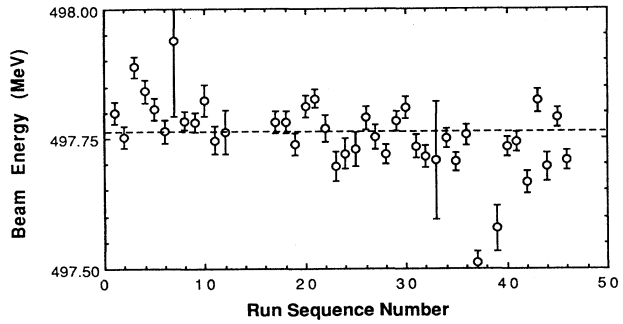

FIG. 4. Distribution of proton-beam energies observed during one of the five data-taking runs. The solid line represents the average energy. The energy scale has not been calibrated absolutely and has an uncertainty of about ±1 MeV.

nematic effects associated with possible lateral movement of the beam on the BEM/polarimeter target. This simple, yet effective, monitor allowed the average beam energy to be checked with an accuracy of ±0.1 MeV in only 10 min of data taking.

The BEM scalers were read every 5 min and proton beam energies were averaged over 2-h periods. A typical distribution of energies during the 2 weeks spanned by one of the five data-taking periods is illustrated in Fig. 4. The largest variation in energy (i.e., width of the stopping distribution) during a 2-h run observed during the experiment was 0.31 MeV FWHM; the largest observed deviation of a single energy determination (2-h period) from the global mean was 0.28 MeV. No data were excluded on the basis of excessive beam energy variation. The average beam energies for the five major data-taking periods were consistent within 0.20 MeV. No corrections to the data were necessary.

B. Secondary neutron beam

The neutron beam was produced via the quasifree $^2\mathrm{H}(\vec{p},\vec{n})2p$ reaction. The neutron production target contained liquid deuterium (LD_2) at 22 K and 168 kPa with a density of 0.167 g/cm^3. Fluctuations in the neutron-beam energy due to LD_2 temperature variations were below ±30 keV. The neutron-beam energy was measured to be 477±2 MeV in a separate experiment. The width of the neutron energy distribution was estimated to be about 11–15 MeV FWHM (Refs. 32 and 33). The neutron beam also has a low-energy tail from $^2\mathrm{H}(\vec{p},\vec{n})2p$ events for which the second final-state proton is no longer simply a spectator. This tail decreases rapidly in intensity below the quasielastic peak to a level of a few percent of the peak intensity.

To denote scattering parameters relevant to the experiment (apart from A_n and A_p) the four subscript notation mentioned earlier is used. Both the neutron-beam production reaction and the CSB measurements involve scattering in the horizontal plane.

The large transverse-polarization transfer coefficient at 9° in the laboratory of the $^2\mathrm{H}(\vec{p},\vec{n})2p$ reaction,[29,34] $(a^2_{0x'x0}+a^2_{0z'x0})^{1/2}\approx 0.78$ ($a_{0z'x0}$ is relatively small, $a_{0x'x0}$ is negative), was used to produce a neutron beam with an x' polarization component of approximately 0.5. In addition, there was a small y' polarization component ($a_{0y'00}=-0.06$) of the neutron beam from the quasifree pn scattering polarization parameter. The neutron beam was extracted at 9° through a 3.37-m-long steel collimator. The magnet which deflected the primary proton beam towards the beam dump also served to sweep charged particles out of the neutron beam. Lead bricks were stacked in the first of the two spin precession dipoles to form a 0.61-m-long secondary collimator. The axis of the primary collimator intersected the proton beam at the center of the LD_2 target and the collimator was constructed to give uniform geometrical transmission coinciding precisely with the length of the LD_2 target.

Two dipole magnets (fields along the $+y'$ and $+x'$ directions) precessed the large x'-z' component of neutron polarization into the vertical direction and the small-y' component (which does not change sign with the primary-proton-beam polarization) antiparallel to the neutron-beam direction. Parity conservation forbids contributions to a left-right asymmetry from longitudinal-polarization components in scattering from an unpolarized target or one polarized normal to the scattering plane. The np elastic scattering spin correlation parameters A_{00xx}, A_{00yy}, and A_{00zz} are even functions of the scattering angle and cannot cause a left-right asymmetry which mimics the effects of ΔA. The spin correlation parameters A_{00zx} and A_{00xz} can influence the A_p measurements if there are polarization components of the neutron beam and the FST in the x'-z' plane. Fortunately, the latter spin correlation parameters are very small[29,34] (A_{00zx} and $A_{00xz}\approx 0.03-0.04$ at 477 MeV and 70° in the c.m.). The error in the neutron spin precession was limited to ±6°. From field measurements on the target axis, the uncertainty in the direction of the proton target polarization from the vertical was approximately 1°. The flaring of the magnetic holding field off the axis results in a radial polarization component which increases to a maximum of about 0.06 P_T at the bottom extremities of the target cell. The spatial average of the radial component over the target volume is zero due to the cylindrical symmetry of the target and the magnetic field. When the uncertainties in the precession of the neutron polarization component due to $a_{0y'00}$ and possible target polarization components in the scattering plane are combined, the effects of A_{00zx} and A_{00xz} influence the ΔA measurement by $<10^{-4}$.

Since the stability of the neutron-beam position was of great importance, the centroids of the x' and y' neutron beam intensity profiles were determined regularly with a neutron-beam profile monitor, located 4.32 m downstream from the FST (16.9 m from the LD_2 target). The origins of recoil protons from a converter scintillator were determined using two delay-line wire chambers (DLC's). The neutron beam has a uniformly illuminated area (<10% variation) of 56 mm by 40 mm at the FST which covers the entire volume of the target cell. The neutron-beam shape remained stable throughout the experiment and the centroids were constant within approximately ±1 mm. This was also consistent with the SEM

information which monitored the proton-beam position stability on the LD_2 target. The stability of the incident neutron beam direction was estimated to be $\pm 0.005°$ which affects ΔA only at the 10^{-5} level.

A neutron-beam polarimeter located just downstream of the profile monitor consisted of four degrader-scintillator telescopes (left, right, up, and down) used to measure the x' and y' polarization components. The left-right "effective" analyzing power of the neutron polarimeter was calibrated while the spin precession dipoles were at their nominal experimental settings to precess the neutron spin into the y' direction. The up-down analyzing power was calibrated while the magnetic fields were set to precess the neutron spin parallel to the x' axis. The effective analyzing powers were $\approx 0.21-0.22$ and differed by about 3% because of the effect of the non-negligible beam dimensions. The observed asymmetries were also very sensitive to movement of the neutron-beam centroid. This provided a second check on the stability of the primary proton-beam position on the LD_2 target.

Neutron-beam polarization components were continuously monitored throughout the experiment. The average $P_{y'}$ was 0.50 and ranged between 0.47 and 0.55. No evidence for any transverse (x') component of the neutron-beam polarization larger than ± 0.01 was found during the experiment.

C. The frozen spin target

A frozen spin polarized hydrogen target (FST) was built specifically for the CSB experiment.[24–26] This type of target allows the proton polarization to be maintained with a smaller magnetic holding field than other types of polarizable targets using butanol as the target material. A small holding field was desired to minimize the bending of the outgoing protons.

The target cell was a 4.0-cm-diameter, 4.5-cm-high cylinder which typically contained 50–55 cm^3 of 1.4-mm-diameter butanol beads immersed in a bath of 94% ^4He and 6% ^3He refrigerant. The volume occupied by the butanol beads in the target canister was determined from x-ray radiographs taken before and after each major data-taking period. Material above and below the inner target canister was kept to a minimum to reduce possible background sources. The neutron beam illuminated the entire inner target canister but not the sides of the outer 8-cm-diameter, 12-cm-high, 1.7-mm-thick aluminum vacuum shell.

Target polarization took approximately 3 h in a 2.6-T magnetic field generated by lifting a superconducting solenoid to surround the target. Once the desired polarization was attained, the temperature was reduced to about 65 mK to "freeze" the polarization. The polarizing field was then reduced to 0.257 T by lowering the superconducting solenoid out of the path of the neutron beam and energizing a conventional solenoid above the target cell. The superposition of the fields from the two solenoids provided a vertical field (within $\pm 1.0°$), reproducible and stable to ± 0.5 mT over a typical 2-week running period. A_n and A_p measurements with the holding field vertically up and down were averaged to reduce the possibility of systematic errors. The proton target polarization could be parallel or antiparallel to the holding field direction and all permutations of field and polarization direction were used.

Target proton polarizations were measured with a nuclear-magnetic-resonance (NMR) system. An NMR coil was located in the center of the target canister. Polarizations were calibrated against thermal equilibrium values in the polarizing field at temperature near 1.6 K. Polarization measurements were made just after the polarization procedure and again about 8 h later at the end of each polarized target cycle. Target temperature was monitored continuously and only one 2-h run showed any anomalous temperature variation. Therefore an exponential decay of polarization between the polarization measurements was assumed. Polarization decay times ranged between 24 h and several hundred hours depending on the target temperature, with typical values of about 100 h. The large variation was due to the very steep dependence of polarization decay time on target temperature and reflected the degree of optimization attained with the refrigeration system before polarization was started. The average target polarization was estimated to be 0.77, varying from 0.90 to 0.50 for individual runs. Comparing the slopes of the A_n and A_p analyzing power data indicated that the target polarizations were free of major systematic errors at the 4% level. This degree of precision is of course useless for a direct measurement of ΔA at the 10^{-4} level.

Displacement of the cylindrical axis of the target canister relative to the axis of the holding field could result in inaccurate reconstruction of both the proton scattering angle (errors in the line integral of the magnetic field over the path length of a recoil proton) and the neutron angle (deviation from the assumed geometry). Radiographs of the target position were made on several occasions over the duration of the experiment. Deviations from the nominal target position in the horizontal plane were less than 2 mm between the major data-collection periods. No significant position differences were noted in any one period. Appropriate corrections were made in the off-line analysis and possible contributions to errors in ΔA are negligible.

D. The proton-detection apparatus

A schematic diagram of the experimental detection apparatus is shown in Fig. 5. The proton detection assemblies were mounted on rigid booms located at $52.00° \pm 0.02°$ to the neutron-beam axis. Each proton detection telescope subtended a laboratory angle range of approximately 11° straddling θ_0. Each boom supported four 58 cm by 58 cm (active area) DLC's for proton-track reconstruction, time-of-flight (TOF) counters for momentum determination, and a range counter assembly to help separate elastic *np* recoil protons from high- and low-energy backgrounds. Each DLC had a single-anode wire plane between two cathode planes and provided both horizontal and vertical coordinates.

The range counter assembly consisted of a ΔE counter,

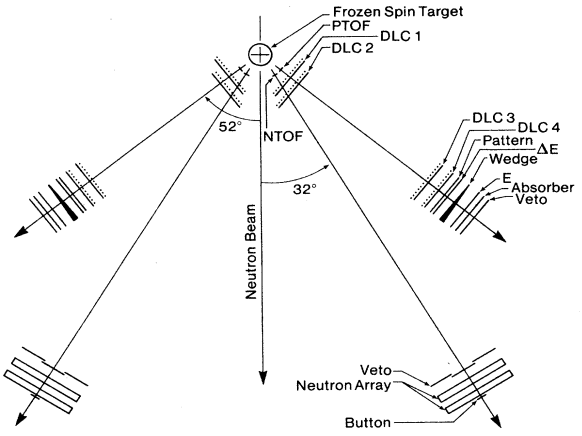

FIG. 5. Schematic diagram of the layout of the experimental detection apparatus showing the positions of the neutron and proton booms relative to the frozen spin target.

a wedge-shaped brass energy degrader which reduced the energies of elastically scattered protons to a common value independent of their recoil angle, the E counter, a thin brass absorber, and a veto counter. The combination of wedge degrader and thin absorber permitted only particles with energies higher than that allowed by free np scattering kinematics to reach the veto counter.

The proton TOF was measured between a small scintillator "start" counter (pTOF) near the FST and a larger "stop" counter (E-counter) 3.4 m away from the FST. The pTOF time signal was taken as the average of the two timing signals from photomultiplier tubes (PMT's) attached to the top and bottom of the counter. Two PMT's viewed the E counter on each of the top and bottom edges. The timing signal from the E-counter was an average of appropriate combinations of either three or four PMT signals and corrections were made for position dependence. Corrections to the calculated proton energies were also made for energy losses in the FST and the wedge-shaped absorber.

The four DLC's on each proton boom were grouped in pairs, one pair near the pTOF and the second pair near the ΔE counter. This gave adequate redundancy and made the system resolution less dependent on wire-chamber inefficiencies. Each chamber provided both horizontal and vertical proton track coordinates from delay lines on the cathode planes. The "picket fence" distributions of the horizontal coordinates allowed an absolute calibration of the nonlinearities of all the chamber delay lines.

The nonlinearities of the chamber delay lines were calibrated in a separate measurement using a different geometry. The four chambers on each boom were grouped together as closely as possible and located on the proton boom as far from the FST as possible. The first and third chambers were rotated by 90° so that their "vertical" coordinate was oriented to give horizontal positions. Protons scattered from the FST were observed over the full active area of the chambers. For the "horizontal" coordinates individual anode wires were easily identifiable as sharp peaks in the delay line time difference spectra (since the anode wires ran vertically). Each peak was matched with its anode wire whose relative positions in space were accurate to ± 0.05 mm. Each "vertical" coordinate was calibrated against the picket-fence spectra of two of the other chambers. The horizontal track position resolution of ± 1.0 mm was limited by the anode wire spacing. The vertical track-position resolution of 0.7 mm FWHM was somewhat better since it was not limited by the granularity of the anode wire spacing.

Acceptable proton tracks in the CSB experiment required at least a single horizontal and vertical coordinate in each of the front and back pairs of DLC's. Approximately 2% of the events did not satisfy this criterion—most of which had no useful DLC data. When coordinates were observed in the central region of two chambers, typical inefficiencies were $<2\%$ in any of the four other individual planes. For events that had valid wire information in at least one chamber, the other chambers usually had valid data and their overall track detection efficiency was $>99.5\%$. Approximately 5% of reconstructed tracks were rejected by later cuts because of excessive multiple scattering which resulted in a poor χ^2 for the fit to a straight line.

Magnetic-field maps of the FST region were made before the beginning and after the completion of the experiment in several planes above and below the median plane of the apparatus. The holding field caused a nominal 1.2° deflection for 156 MeV protons scattered at 52° from the center of the FST. The actual deflection depended on holding field direction, the np vertex position within the target, the proton recoil energy, and the proton energy loss in the target material and support structure. The fringe field near the FST of the neutron-beam spin precession dipole magnets was about 1.1 mT in the x' direction. The vertical fringe field of the cyclotron was about 0.5–1.0 mT at the FST. Over the length of the proton detection apparatus the integrated cyclotron field was 1.24 mT m, approximately 3% of the holding field line integral. To understand the effects on the detection system, simulated "average" proton paths were tracked in the holding field from an assumed position at the center of the FST through the DLC's. The small transverse magnetic field components were neglected in the analysis. The simulation included the effects of average proton energy losses through the system. The results of the simulation were used to define a momentum-dependent correction to the observed proton angle.

An additional proton angle correction of about 0.1° was made for experimental biases caused by a combination of nuclear interactions in the wedge-shaped absorber, the target holding field, and multiple scattering in the target. Protons at a given angle which multiple scattered towards the thick side of the wedge had a larger nuclear interaction probability than those which multiple scattered towards the thin side, producing a statistical bias towards larger scattering angles. The observed instrumental biases were reproduced qualitatively using a Monte Carlo simulation. The actual corrections were taken from the mean experimentally observed error in the

np opening angle distributions for tightly constrained elastic scattering events. Separate corrections for *left* and *right* events and for field *up* and *down* were used. This also provided an empirical compensation for the effects of the cyclotron fringe field.

The small biases observed in the proton angle distributions do not by themselves have any effect on the measurement of ΔA since both the A_n and A_p distributions are affected to the same extent. The corrections were done so that a consistent statistical analysis could be made for all events in order to discriminate against (n,np) background.

E. Neutron-detection apparatus

The neutron-detection assemblies were centered at $32.00°\pm0.02°$ relative to the neutron-beam axis and subtended an 11.4° angular range. Each neutron detector included two stacks of seven optically isolated NE110 scintillator bars 1.05 m wide, 0.15 m deep, and 0.15 m high. The bars were fitted with modified Winston cone light collectors and photomultipliers at each end. This geometry accepted light reflected from the inside surfaces of the bars at angles $\leq 15°$. Groups of either three or four nonadjacent PMT's on one side of a scintillator stack were connected electrically as illustrated in Fig. 6 which shows the neutron-array electronics. The delay line "daisy chain" allowed time information to be used to identify the bar in which the neutron interaction occurred and minimized the electronics required. Three overlapping scintillation counters were placed in front of the neutron array in order to veto charged particles. Small 70-mm-by-64-mm "button" counters were located behind the center of each scintillator bar of the back array. The neutron-array pulse-height (PHT) signals for the passing protons which penetrated to the button counters were used to calibrate the gain and timing characteristics of the scintillator-array PMT's on a run-by-run basis. These "button events" were obtained concurrently with the *np* elastic-scattering data. They were analyzed in a first pass through the data to provide the necessary calibrations and corrections for timing and gain fluctuations. A counter (*n*TOF) similar to the *p*TOF was used to select charged particles coming from the FST region.

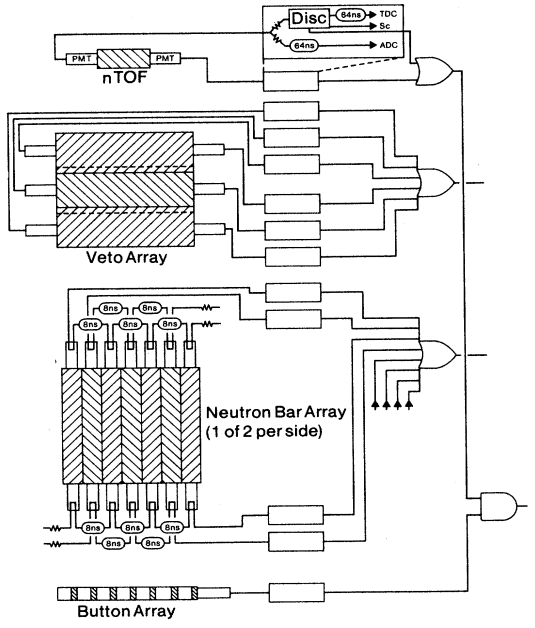

FIG. 6. Schematic diagram of the neutron-detection system electronics preceding the trigger logic. The "daisy-chain" arrangement of nonadjacent groups of three and four neutron scintillator bars allows the bar in which the neutron interacts to be identified with a minimum of electronic modules. The *n*TOF and button counters detect fast protons which penetrate the neutron scintillator bars.

The neutron-detection efficiency was initially dependent on the hardware threshold of the electronic discriminators and later on, in the off-line analysis, on the software pulse-height thresholds which exceeded the hardware limits. Shifts in the photomultiplier gains without a corresponding rescaling of the software discrimination thresholds would change the neutron detection efficiency. Button events provided a statistically stable signal from the photomultipliers against which gains were calibrated. The button protons deposited about 60 MeV in the neutron-scintillator bars. The PHT centroids were maintained at their nominal values by periodic adjustments of the high voltages. Drifts in gain between consecutive 2-h periods for each of the 56 PMT's could be determined to within about $\pm0.3\%$. The average scattering angle (and therefore the energy distribution) of the button protons was slightly dependent on the deflection of the particles in the FST holding field. Button event pulse heights were scaled by approximately $\pm0.7\%$ depending on the field direction to compensate for this effect.

The x' coordinate of the interaction point in the neutron scintillator bar was determined from the difference of the time signals from opposite ends of the struck bar. The lengths of the bars corresponded to a time difference range of 13.2 ± 0.2 ns. Relative timing drifts of the PMT's at either end of a bar affected the position determination. The discrepancies between the apparent button proton positions and the physical button counter locations were used to correct for these drifts for each bar. The centroids of the button proton positions were determined to within ±0.4 mm during each 2-h data-taking run.

Uncertainties in the y' and z' neutron interaction coordinates both were limited to ±7.5 cm by the 15-cm height and depth of the neutron scintillator bars. The position resolution along the bars was estimated to be 30 mm FWHM from the difference of the observed positions of individual button events in the front and back bars.

Neutron time-of-flight information was determined from the time of the scattering at the FST calculated using *p*TOF information and the average of the timing signals from the struck neutron scintillator bar. The effects of timing drifts on the extracted particle energies were monitored using *np* elastic events. The deviations of the proton and neutron energies from the values expected by kinematics (derived from the angle information) were

determined on a run by run basis. Timing corrections were made to keep the centroids of the *np* elastic neutron energy deviations for each bar smaller than 2 MeV. The timing resolution in the neutron arrays did not always allow unambiguous identification of the original neutron scintillator bar struck when the interaction products were detected in adjacent bars. In such cases the interaction times in the two bars were averaged and a small timing correction applied to obtain properly calibrated energies.

F. Data collection

The experimental data taking spanned 11 months, including four 2-week periods using butanol and a final 1-week period with graphite in the FST to determine the inelastic background. During successive 4-day-long cycles, data were collected with target polarization up and down and unpolarized neutron beam, and with polarized neutrons and an unpolarized target. The holding field was also used in both vertical directions. Each 4-day cycle included all permutations of beam and target polarizations, and holding field direction. During the polarized beam portions of the experiment, the proton-beam polarization was cycled at random under computer control between up, down, and unpolarized states, the ratio of times being 3:3:1 for the different states.

Numerous on-line checks were made by the acquisition program to monitor the operation of the FST, position stability of the proton and neutron beams, the proton-beam energy and polarization, and the reliability of the particle detection apparatus. The long-term stability of the equipment was monitored with an off-line analysis that provided feedback within several hours. In this off-line analysis PHT drifts in the neutron detectors and the efficiencies of wire chambers were checked. High-voltage adjustments to the neutron counters were made if any gain drifts exceeded a few percent.

III. ANALYSIS

The full data analysis progressed through four stages: (i) calibration of equipment on a run-by-run (tape) basis with special attention paid to understanding all possible sources of systematic errors; (ii) selection of *np* elastic events based on a statistical analysis of the kinematic parameters of each event; (iii) calculation of scattering asymmetries from the angular distributions to extract the zero-crossing angles and ΔA, and (iv) study of the inelastic background and correction to the extracted value of ΔA. Most of the procedures used for calibration of the apparatus have been described above.

A. Selection of neutron-proton elastic events

Neutron-proton coincidences were detected in mirror-symmetric pairs of neutron and proton detection telescopes. Events will be referred to as "left" or "right" according to the side of the neutron beam on which the scattered neutron was observed (from the point of view of an observer looking downstream).

For *np* elastic scattering in the laboratory, assuming the incident energy to be known, only two kinematical variables (including one azimuthal angle ϕ_p or ϕ_n) need to be observed to calculate all the parameters of an event. Since all of the following observables were measured: T_p, T_n, θ_p, θ_n, ϕ_p, and ϕ_n, each event was four times kinematically overdetermined. This overdetermination allowed *np* elastic events to be distinguished from inelastic background. χ^2 variables were defined for the following kinematic parameters: the sum of the neutron and proton kinetic energies, $T_{\rm sum}=T_p+T_n$; the x' component of the sum of the particle momenta, $P_{x'}=(\mathbf{p}_p+\mathbf{p}_n)_{x'}$, the *np* opening angle, $\theta_s=\theta_p+\theta_n$; and the *np* azimuthal coplanarity, $\Delta\phi\equiv\phi_n-\phi_p-180°$.

A typical $T_{\rm sum}$ histogram for elastic events is illustrated in Fig. 7(a). The nominal neutron-beam energy was 477 MeV. The 14-MeV FWHM spread in the incident neutron energy distribution, the spread of proton energy losses in the FST, and the resolution of the scattered neutron TOF were the main contributors to uncertainties in $T_{\rm sum}$. The tail below the peak is due to a low-energy component in the incident neutron energy distribution and the (n,np) background not rejected by cuts on the other kinematic parameters.

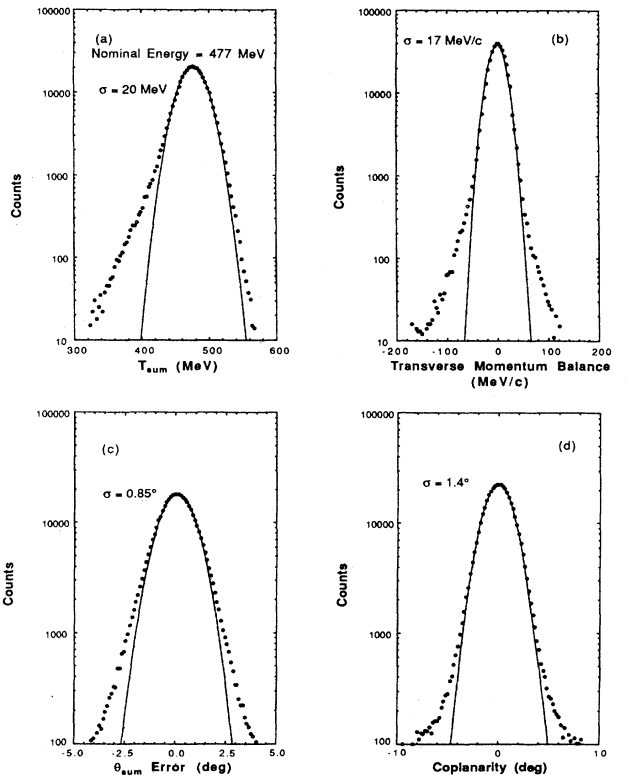

FIG. 7. Distributions of the kinematic variables used for χ^2 tests. In all cases events are selected by requiring $\chi_i^2<5$ for the three other kinematic parameters. The solid curves are Gaussian distributions with the standard deviations determined from fits to the central regions. (a) *np* kinetic energy sum. The centroid is equal to the energy of the incident neutron-beam energy. With χ^2 cuts applied, the low-energy tail is mainly due to the incident neutron-beam energy distribution, and only partly due to (n,np) reactions. (b) *np* horizontal momentum balance. (c) Deviation between the observed and kinematically expected *np* opening angles. (d) Experimental *np* coplanarity.

An example of $P_{x'}$ is illustrated in Fig. 7(b). For elastic scattering, even for low-energy incident neutrons, the total transverse momentum of the scattered *np* pair should be zero. Constraints on P_x eliminate only (n,np) events.

The deviation between the observed *np* opening angle in the laboratory and the kinematically expected value, $\Delta\theta_s$ is illustrated in Fig. 7(c). The width of the elastic scattering distribution is due primarily to Coulomb multiple scattering of the protons in the FST. Constraints based on $\Delta\theta_s$ eliminated (n,np) events, double-scattered nucleons, and elastic-scattering events originating from the low-energy neutrons in the beam.

For *np* elastic scattering the neutron and proton azimuthal angles should differ by 180°. The coplanarity variable $\Delta\phi$, defined as the deviation from 180°, is shown in Fig. 7(d). The width of $\Delta\phi$ is dominated by proton multiple scattering and then ± 7.5 cm uncertainty in the neutron vertical interaction position due to the size of the neutron scintillator bars. Only (n,np) events and double-scattered nucleons are eliminated using this observable.

Assuming a nominal neutron-beam energy of 477 MeV, the statistical quality of each event was evaluated by defining χ^2 variables for the four observables presented in Fig. 7. The standard deviations for the distributions were obtained from the data. Adjustments to the standard deviations were made on an event-by-event basis to compensate for the angle dependence due to the large relative variation in the proton energy over the acceptance of the detection system. The standard deviations varied from their central values by approximately $\pm 10\%$.

The observed low-energy tail in Fig. 7(a) is due primarily to low-energy neutrons in the incident beam. A θ_s distribution for the events in the tail of Fig. 7(a) shows a very strong bias to large opening angle and is consistent with $>90\%$ of them being *np* elastic scattering. The $T_{\rm sum}$ tail is cut off below 300 MeV by the constraint on θ_s. The $T_{\rm sum}$ distribution of (n,np) events peaks at 455 MeV, with the distribution falling to a relatively flat level below 380 MeV of about 20% of the peak value. Based on the width of the coplanarity distribution, a standard deviation of about 0.75° was expected for $\Delta\theta_s$. The observed width of 0.85° is consistent with an effective energy spread in the neutron beam of about 10–20 MeV. A positive bias of about 0.1° in the centroid of the $\Delta\theta_s$ distribution, which is not readily apparent in Fig. 7(c), is also due to the effect of neutrons with energies below the nominal value.

Several different combinations of constraints on the χ^2 variables were used in the analysis to verify that the experimental result was not dependent on the value and/or type of cut. In some cases, all four χ^2 variables were forced to be less than a specific value. This condition is expressed as $\chi_i^2 < \eta$. Alternatively, constraints were applied to the sum of the four χ_i^2 variables; this constraint is expressed as $\sum \chi^2 < \xi$. Distributions of the $\sum\chi^2$ variable and of one of the simple χ_i^2 variables are illustrated in Fig. 8 for all observed *left* events. There are no constraints applied to the data. In the experiment about 10% of the triggers are due to scattering of neutrons with energies less than 440 MeV. Nearly 75% of all triggers

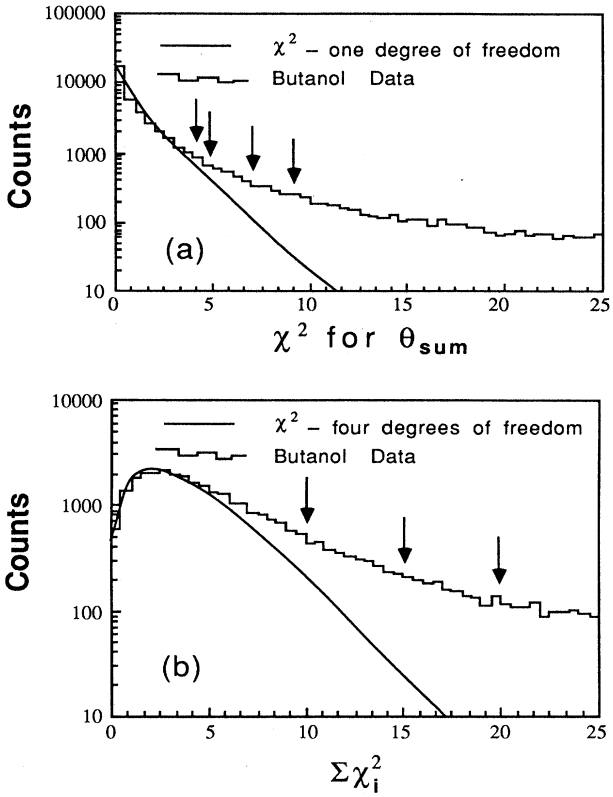

FIG. 8. (a) The *np* opening-angle error χ^2 distribution for all left events. An ideal χ^2 distribution with one degree of freedom is illustrated by the solid curve. Note the larger tail of the experimental χ^2 distribution. This is primarily due to (n,np) events with some contribution from the energy distribution of the incident neutron beam. The positions of the χ^2 constraints at 4, 5, 7.5, and 9 used in the analysis are indicated by arrows. (b) The $\sum\chi^2$ distribution compared to an ideal χ^2 distribution with 4 degrees of freedom. The arrows indicate the constraints at 10, 15, and 20 used in the analysis.

were *np* elastic events and the remaining events were (n,np) reactions on nuclei. The various cuts employed in the analysis, $\sum\chi^2 < 10$, 15, or 20, and $\chi_i^2 < 4$, 5, 7.5, or 9, are also illustrated on the figure. The constraint $\chi_i^2 < 5$ employed for the quoted result allowed about 1% background in the elastic *np* event sample and accepted approximately 85% of elastically scattered *np* events. The distributions displayed in Fig. 8 deviate from ideal χ^2 distributions because of non-Gaussian multiple scattering in the target, the low-energy component in the incident neutron beam, and the presence of (n,np) background.

For cases where there was redundant proton track information from the DLC data, a "goodness of fit" variable $\Delta^2 = \sum (x_r - x_0)^2/(N-4)$ was determined. x_r and x_0 are the reconstructed and observed DLC coordinates, and $(N-4)$ is the number of coordinates used in the track-reconstruction calculation minus the four coordinates necessary to reconstruct a track. The sum was over the valid horizontal and vertical DLC coordinates among the eight possible. A cut was placed at $\Delta^2 \leq 40$ which rejected $\sim 5\%$ of the recorded events coming from the FST target region. This loose cut eliminated only events with

large multiple scattering in individual DLC's or where there were multiple hits in the chambers.

The z'-y' projection of the np vertex image was calculated from the DLC proton track information. The cuts placed at $|y'| \leq 30$ mm and $|z'| \leq 35$ mm were very liberal and only removed background events. These constraints on the target image z' coordinate were intentionally loose since no corrections were applied to the vertex reconstruction to account for the deflection of the protons in the magnetic holding field of the FST. The reconstructed target image was displaced by ± 3 mm along the beam direction depending on the side of the beam on which the proton was detected, and on the holding field orientation.

The proton telescopes determined the geometrical acceptance for np elastic scattering events. Only a small fraction of the top and bottom neutron scintillator bars, varying from about 8% for the small neutron scattering angles to less than 1% at the larger angles, was inside this geometrical acceptance. Since so few elastically scattered events were observed in the top and bottom bars, they contributed a disproportionate number of (n,np) events. Therefore, all events detected in the top and bottom bars were excluded from the data set used to calculate the zero-crossing angles for A_n and A_p.

A typical normalized neutron scintillator bar PHT spectrum with the ADC pedestal subtracted is shown in Fig. 9. The hardware discrimination threshold is in a region where the PHT distribution is rising rapidly. In order to check for possible systematic errors associated with gain changes in the neutron array PMT's or variations in the hardware discrimination thresholds, asymmetry zero-crossing angles were calculated as a function of several software cuts on the PHT's. Cuts were applied at the ADC channels 0, 15, 20, and 25 and compared. No systematic effects were found even without software discrimination (ADC channel zero as the lower limit).

B. Asymmetry calculation

The principle of extracting $\Delta A = A_n - A_p$ from the difference between the zero-crossing angles is illustrated in Fig. 1. The constant of proportionality is the c.m. slope of the analyzing power

$$A_n - A_p = -\Delta\theta \frac{dA}{d\theta} . \tag{8}$$

After constraints were applied the events were sorted into histograms with 0.25° (lab) wide bins for θ_p and θ_n. The left-right scattering asymmetries were then calculated on a bin-by-bin basis and the slopes of the asymmetries and the zero-crossing angles determined with a linear least-squares fit. For convenience the results were expressed in terms of the equivalent c.m. neutron scattering angle.

Several procedures were used to determine ΔA. In the procedure referred to as the "overlap" calculation the scattering asymmetry is obtained from

$$\epsilon = \frac{r-1}{r+1} , \tag{9}$$

where r is the ratio

$$r = \left[\frac{L^+ R^-}{R^+ L^-} \right]^{1/2} . \tag{10}$$

The superscript represents the proton or neutron polarization direction for measurements of A_p or A_n. This method of calculation cancels all systematic errors not correlated with target or beam polarization reversals to at least first order. However, the procedure is only possible for the angle range common to both left and right scattered protons. This was approximately 9.5° (lab) because of the effect of the target magnetic holding field.

Asymmetries were also calculated for *left* and *right* events separately over a larger 11° (lab) range where the number of events in every angle bin was greater than 50. The scattering asymmetry in these cases was given by

$$\epsilon_L = \frac{L^+ - \kappa L^-}{L^+ + \kappa L^-} \tag{11}$$

for left events, and

$$\epsilon_R = \frac{R^+ - \kappa R^-}{R^+ + \kappa R^-} \tag{12}$$

for right events. The constant κ, used to obtain the correct relative yield normalization, is the ratio of the total number of events detected for polarization up and polarization down in the central 8° (lab) where the acceptance was uniform within ±3%:

$$\kappa = \frac{L^+ + R^+}{L^- + R^-} (\text{central } 8°) . \tag{13}$$

The "nonoverlap" calculation benefits from improved statistics but is potentially more susceptible to systematic errors. A comparison of the asymmetries calculated via the two methods provides a means of testing consistency between the left and right detection systems and is a control for systematic effects since errors generally enter into the separate calculations in a different manner.

The analyzing-power zero-crossing angle can be deter-

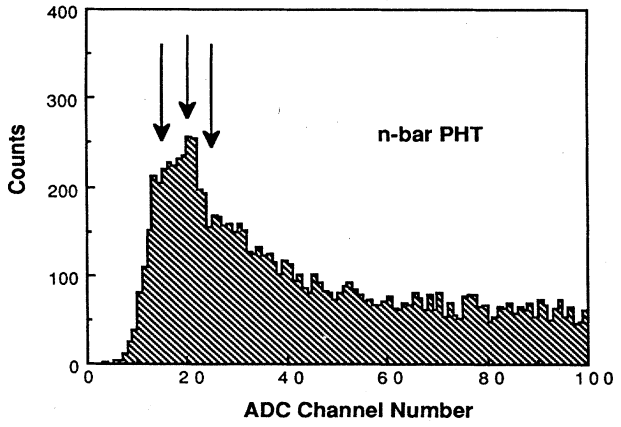

FIG. 9. A typical neutron scintillator bar phototube ADC response after pedestal subtraction and gain renormalization. The arrows indicate the PHT cuts at 15, 20, and 25 channels used in the analysis.

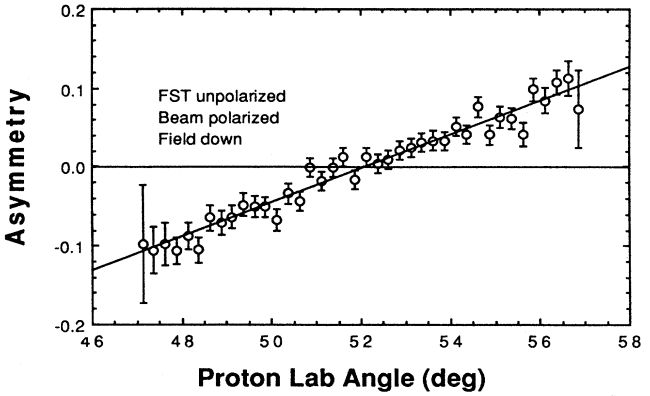

FIG. 10. A typical scattering asymmetry angular distribution calculated with the overlap method. A linear least-squares fit to the data is displayed. The data shown were obtained during the first data-taking run with the magnetic holding field pointing down, neutron-beam polarized, and FST unpolarized. Note that the laboratory scattering angle is used here.

mined from the scattering asymmetry distribution as a function of either θ_n or θ_p. The analysis concentrated on the proton angle result because measurement of neutron angles is susceptible to a number of additional systematic and random errors (discussed later).

A typical scattering asymmetry angular distribution is illustrated in Fig. 10 along with its linear least-squares fit using the zero-crossing angle and the slope as free parameters. All major runs were analyzed separately to avoid the introduction of systematic errors. Separate fits (a total of 48) were made for A_n and A_p data for each FST field direction before the results could be combined. The distribution of confidence levels for the fits was flat so their quality was considered satisfactory. Simulations showed that no systematic error in determination of the difference between the A_n and A_p zero-crossing angles is introduced by ignoring deviations from linearity in this limited angle range. Zero-crossing angles will be denoted by θ_{0p} when the data are obtained from proton scattering angles and θ_{0n} when the neutron scattering angles are used. The differences between the zero-crossing angles are denoted by $\Delta\theta_p = \theta_{0p}(A_n) - \theta_{0p}(A_p)$ and $\Delta\theta_n = \theta_{0n}(A_n) - \theta_{0n}(A_p)$.

C. Investigation of systematic errors

The values of $\Delta\theta_p$ averaged over the holding field directions for the four *np* elastic scattering data taking periods are listed in Table I. They are consistent, as are measurements made with different holding fields. The small differences between the nonoverlap and overlap calculations using the proton scattering angles indicate that systematic errors associated with the angle range used in the fit are under control at the 0.06° level. The comparable difference for neutron angles was less than 0.01°. The results for the nonoverlap region include portions of the system where there was rapid variation in detection efficiency and the potential for systematic errors is large. The difference in Table I between the overlap and nonoverlap calculation, especially when the neutron angle results are considered, is indicative the good control over systematic errors, but is not a measure of systematic error in the quoted results. When the proton angle range used for the two modes of calculation was the same, the mean difference was only 0.004°. There is no indication of any uncorrected systematic effect that affected the left and right events differently.

The asymmetry zero-crossing angle was also determined from the neutron scattering angle distributions. Comparison of $\Delta\theta_p$ and $\Delta\theta_n$ is shown in Table II. In the c.m. system $\Delta\theta_p$ should be equal to $\Delta\theta_n$. The agreement is reasonable.

As stated earlier, some undesired polarization components could potentially affect measurement of ΔA. The target configuration, the choice of beam and target spin combinations, and the care in preparing the beams make contributions to ΔA from A_{00xx}, A_{00yy}, A_{00zz}, A_{00zx}, and A_{00xz} completely negligible, even in the most pathological cases (which are known not to have occurred since the transverse neutron polarization components were measured continuously). The FST subtends an angle of only $\pm 0.1°$ at the LD_2 target so the spatial nonuniformity of the neutron-beam polarization profile is

TABLE I. Difference between the A_n and A_p zero-crossing angles, $\Delta\theta_p$ in the c.m., based on the proton scattering angles. Constraints applied are $\chi_l^2 < 5$, and PHT > 20. The column of nonoverlap values is the weighted average of the left and right events. The error in the least significant digits is given by the value in brackets. The error for the nonoverlap-overlap difference is an estimate taking into account the correlation in the data sets. The values have not been corrected for background.

	Simple average over FST magnetic holding fields $\Delta\theta_p$ (c.m. degrees)				
Run	Left events	Right events	Nonoverlap region	Overlap region	Nonoverlap-overlap difference
1	0.723(440)	0.685(430)	0.704(307)	0.659(316)	+0.045
2	0.293(496)	0.480(469)	0.392(341)	0.444(347)	−0.052
3	0.156(328)	0.230(336)	0.192(235)	0.086(245)	+0.106
4	0.602(424)	0.270(428)	0.437(301)	0.356(299)	+0.081
Weighted average	0.404(204)	0.387(203)	0.396(144)	0.340(147)	+0.056(40)

TABLE II. Comparison of the A_n and A_p zero-crossing angle differences, $\Delta\theta_p$ and $\Delta\theta_n$ in the c.m. The values are obtained from the simple average over the two FST magnetic holding field directions. Constraints applied are $\chi_i^2 < 5$, and PHT > 20. The values for the overlap region have been used. The background analyzing power assumes a neutron-beam polarization 0.51±0.01 and the correction is made using Eq. (15).

	$\Delta\theta$ (c.m. degrees)		
	$\Delta\theta_p$		$\Delta\theta_n$
$\Delta\theta$ for run 1	+0.659(316)		+0.762(313)
$\Delta\theta$ for run 2	+0.444(347)		+0.442(342)
$\Delta\theta$ for run 3	+0.086(245)		+0.194(240)
$\Delta\theta$ for run 4	+0.356(299)		+0.480(304)
Weighted average	+0.340(147)		+0.429(146)
Background analyzing power (A_b)	+0.004±0.085		+0.026±0.085
Background fraction (r_b)		0.010±0.003	
Background-corrected $\Delta\theta$	+0.340(162)		+0.414(161)
$dA/d\theta$		−0.01382	
ΔA	+0.0047±0.0022		+0.0057±0.0022

small. Systematic effects from this source, and from possible nonuniformities in the target polarization cancel because left and right scattered events were observed concurrently.

The proton range telescope wedge contributed a small systematic error to the measurement of θ_p as discussed in Sec. II D. Corrections for this were made, and as for most systematic errors, the effects cancel when the CSB difference $\Delta\theta_p$ is formed. The ratio of detection efficiencies for left and right events was constant within statistical errors of about ±2% in the central 6° (lab) of the system acceptance, but the left and right event efficiencies differed in relative value by about 15% because of nuclear interactions in the wedge degrader. The ratio of efficiencies changed from 0.85 to 1.15 when the FST magnetic holding field was reversed. Simulation of the presence of the wedge in the system did not produce any bias in $\Delta\theta_p$.

Asymmetries were determined for a variety of χ^2 cuts. The χ^2 cuts were selected to accept a large percentage of *np* events while reducing quasielastic background to a level where it had minimal effect on the asymmetry calculation. Table III shows the results of various χ^2 constraints on the data set. There is no significant dependence on the details of the χ^2 cut. This is consistent with the effect of background contamination being small, in agreement with other considerations that will be described later.

Table IV contains values of $\Delta\theta_p$ as a function of cuts on the neutron scintillator bar PHT's after corrections for gain shifts and the ADC pedestals. The PHT cut at ADC channel 20 employed in the final results is just above the hardware discrimination threshold for all the neutron counters. It yields maximum detection efficiency but avoids possible systematic effects due to variations in the hardware threshold due to PMT gain changes or electronic drifts. The absence of any systematic dependence of $\Delta\theta_p$ on the PHT discrimination threshold indicates that it does not influence the result.

D. Background subtraction

The most serious potential source of error in the measurement of ΔA arises from the presence of (n,np) events from the nonhydrogenous materials in the path of the neutron beam. Inelastic processes influence the A_n mea-

TABLE III. A_n and A_p zero-crossing angle differences $\Delta\theta_p$ in the center of mass, based on the proton scattering angles using several different χ^2 constraints. The data for different magnetic holding fields have been averaged together. No background corrections have been made.

	$\Delta\theta_p$ (c.m. degrees)						
Constraint run	$\chi_i^2 < 4$	$\chi_i^2 < 5$	$\chi_i^2 < 7.5$	$\chi_i^2 < 9$	$\sum\chi^2 < 10$	$\sum\chi^2 < 15$	$\sum\chi^2 < 20$
1	0.807(338)	0.659(316)	0.661(292)	0.701(289)	0.798(300)	0.556(287)	0.595(286)
2	0.563(355)	0.444(347)	0.429(323)	0.484(317)	0.450(333)	0.478(316)	0.454(316)
3	0.023(259)	0.086(245)	0.093(226)	0.154(222)	0.017(235)	0.136(224)	0.134(220)
4	0.374(312)	0.356(299)	0.365(283)	0.388(227)	0.413(289)	0.358(278)	0.378(273)
Weighted average	0.376(154)	0.340(147)	0.342(137)	0.387(135)	0.363(141)	0.343(135)	0.349(133)

TABLE IV. A_n and A_p zero-crossing angle differences, $\Delta\theta_p$ in the c.m. based on the proton scattering angle using different constraints on the neutron scintillator bar pulse heights. The data for different magnetic holding fields have been averaged together. (MeV ee≡ MeV electron equivalent).

	$\Delta\theta_p$ (c.m. degrees)			
Run	No PHT cut	PHT >ch15 (0.84 MeV ee)	PHT >ch20 (1.12 MeV ee)	PHT >ch25 (1.4 MeV ee)
1	0.684(303)	0.618(309)	0.659(316)	0.656(322)
2	0.378(325)	0.470(337)	0.444(347)	0.402(354)
3	0.063(234)	0.000(241)	0.086(245)	0.129(252)
4	0.339(291)	0.299(294)	0.356(299)	0.352(302)
Weighted average	0.321(141)	0.292(144)	0.340(147)	0.348(150)

surement if the quasielastic scattering processes, for example, $^{12}C(n,np)$, $^{3,4}He(n,np)$, and $^{16}O(n,np)$, have nonzero asymmetries at the elastic scattering zero-crossing angle. Estimates of background effects were made by replacing the butanol target beads with graphite beads during the final data taking period to create a dummy target. This removed most of the hydrogen from within the target but retained the relative mass ratios of the various background sources. It was assumed that the effects of carbon and oxygen in the FST are equivalent in producing background events. Sources of background within the FST viewed by the proton time-of-flight system are listed in Table V.

The number of (n,np) events from target material and support structure was minimized by the design of the apparatus. Together, the wedge-shaped energy degrader and the veto counter allowed protons with energies more than 20 MeV from that expected for *np* elastic scattering kinematics to be eliminated. The sides of the FST vacuum walls were outside the limits of the collimated neutron beam. The acceptance of the *p*TOF-*E* counter combination excluded that part of the vacuum wall intercepted by the beam when entering or exiting the target. Material immediately above and below the target container was also minimized to reduce background. Constraints on kinematic observables further reduced quasielastic scattering contamination.

Some modifications to the data-collection procedures and analysis were necessary for the background run. There were an insufficient number of button events to obtain the required accuracy for the usual PHT and timing calibrations. More important, the energy distribution of protons produced from the $^{12}C(n,pX)$ reaction differed in an unknown manner from that for *np* elastic scattering. The required button events were obtained midway through the background run by attaching a special polyethylene (CH_2) collar to the FST. Drifts during the final measurement were small and were ignored. However, energy calibrations were less precise than for the butanol target runs.

The background changes the true A_n such that

$$A_n(\text{true})=\frac{A_n(\text{measured})-r_b\,A_b(\text{measured})}{1-r_b}\ , \quad (14)$$

TABLE V. Sources of background in the frozen-spin target.

Item	Material	Density (g/cm^3)	Thickness (cm)	Radius (cm)	Mass (g)
Refrigerant	Helium[a]	0.075[b]	2.00	2.0	5.2
Microwave cavity	Copper	8.96	0.005	2.0	3.1
Teflon sleeve	Teflon (CF_4)	2.2	0.013	2.0	2.0
Inner vacuum can	Stainless steel	7.87	0.038	2.2	22.7
Insulation	Mylar ($C_5H_4O_2$)	1.39	0.001	2.4	0.1
Inner heat shield	Copper	8.96	0.013	2.5	10.1
Insulation	Mylar ($C_5H_4O_2$)	1.39	0.003	2.5	0.2
Middle heat shield	Aluminum	2.70	0.013	2.8	4.1
Insulation	Mylar ($C_5H_4O_2$)	1.39	0.013	3.4	2.1
Outer heat shield	Aluminum	2.70	0.013	3.4	0.1
NMR coil[c]	Copper	8.96			4.3
Resistor[d]	Graphite-epoxy	1.2			0.1
Total mass of nontarget material					54.1
Butanol (C_4H_9OH)	(^{12}C and ^{16}O only)	(Normal run)			24.8±1.3
Carbon		(Graphite-target run)			29.7±0.1

[a]A solution of 6% ^{3}He and 94% ^{4}He.
[b]A packing fraction of 0.6 was assumed.
[c]A 0.051-cm-diameter, 3-cm-long copper wire at the target center.
[d]0.082-cm^3 resistor, located in the base of the target canister.

where r_b is the ratio of background rate to the total observed event rate and $A_b = \epsilon_b / P_{\text{beam}}$ is the background effective analyzing power with a polarized neutron beam. P_{beam} is the neutron-beam polarization. The factor $r_b A_b$ should remain $< 10^{-3}$ if corrected background effects on ΔA are to remain negligible compared to the experimental statistical accuracy. An unpolarized neutron beam impinging on unpolarized target nuclei does not produce any left-right scattering asymmetry. Therefore background events only decrease the slope of the observed $\epsilon_p = A_p P_T$ asymmetry distribution (appearing to reduce the effective FST polarization, P_T), but do not affect the actual determination of θ_0.

It was impossible to determine reliably the contamination fraction r_b from the butanol data alone. Even at large χ^2, background events cannot be distinguished unambiguously from *np* elastic scattering events. Non-Gaussian proton multiple scattering and the low-energy tail in the incident neutron energy distribution cause the observed event χ^2 distributions to deviate from the ideal case.

Ideally, in the background run all hydrogen should have been removed from the FST so as to observe only the contribution from inelastic events. Unfortunately, small amounts of hydrogen remained within the graphite target and *np* elastic scattering events dominate the data sample because of the large *np* elastic scattering differential cross section. The primary sources of hydrogen in the graphite target were a resistor located in the base of the target canister (used as a thermometer), and the Mylar superinsulation around the target walls. The epoxy resistor contained approximately 11 mg of hydrogen. To eliminate the majority of the *np* elastic events, the target was subdivided into two sections during the off-line analysis using the reconstructed proton tracks. Only events originating from the top half of the target were used to estimate the background.

Several procedures were used to check the ability to estimate the background contribution in the *np* data sample. The dependence on the χ^2 cuts is most easily seen by examining $\sum \chi^2$. $\sum \chi^2$ distributions for events detected from the top and bottom halves of the graphite bead-filled target are illustrated in Fig. 11. In Fig. 11(b) there is a pronounced peak due to *np* elastic scattering events from the epoxy resistor. A sample $\sum \chi^2$ distribution from the butanol target is shown in Fig. 11(c) for comparison. The estimated contribution from (n,np) background is also shown in Fig. 11(c). The normalization of the curve assumes that all events with $\sum \chi^2 > 40$ are due to (n,np) reactions. Since there are neutrons with energies < 360 MeV in the beam, this overestimates the background. The effect of a $\sum \chi^2$ cut on the loss of good *np* elastic events and the fractional background contamination is demonstrated in Fig. 12. This figure is derived from the results shown in Fig. 11(c). For a cut $\sum \chi^2 < 10$, the background would be $\leq 2\%$. This constraint is slightly less restrictive (more background) than the constraint $\chi_i^2 < 5$ actually applied to select the *np* elastic events.

The second procedure to estimate the background used the observed event coplanarity. It assumes that the very noncoplanar events in the butanol-filled target data are due to (n,np) processes. A plot of the *np* coplanarity produced from the butanol is shown in Fig. 13. All events in the top histogram are from data taken with the butanol-filled FST. The cut $\chi_i^2 < 5$ was applied to the three other kinematic observables to reduce the inelastic contribution. Scaled data from the top half of the graphite target are shown in the center distribution for comparison. An elastic scattering peak atop a wide, relatively flat background is seen. Events from the butanol target which triggered the proton telescope veto counter are shown in the lower curve. Outside the region of the elastic peak

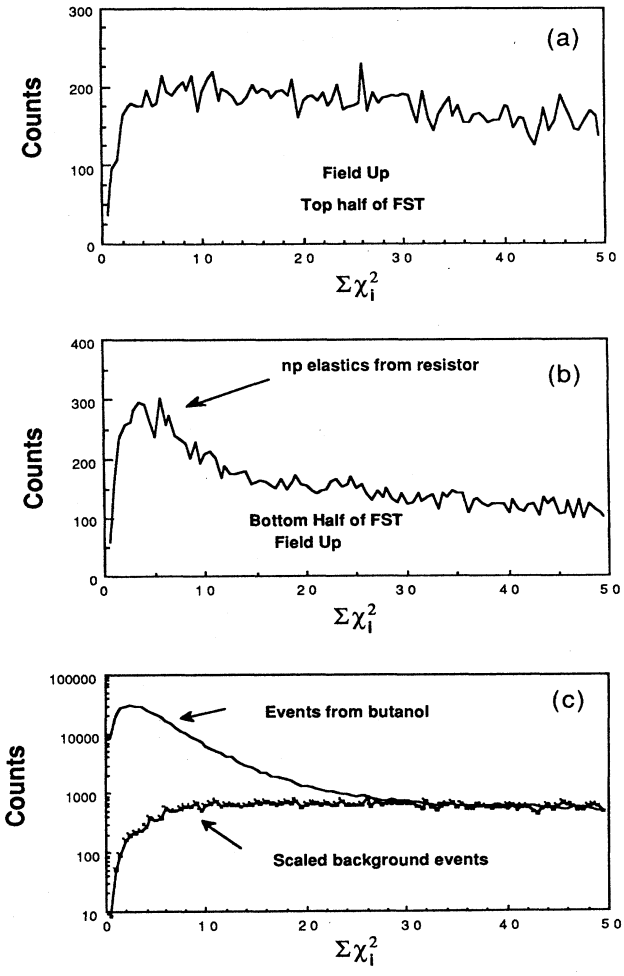

FIG. 11. (a) The $\sum \chi^2$ distribution of events collected from the top half of the target during the graphite-target run. (b) The $\sum \chi^2$ distribution of events collected from the bottom half of the graphite target. The *np* elastic peak is more pronounced here than in (a) because of the presence of an epoxy resistor in the base of the target canister. The tail is lower because a screen inserted into the target to prevent the carbon beads from blocking the He pumping lines did not allow the bottom of the target to be completely filled. (c) The $\sum \chi^2$ distribution of all events collected with the butanol target. The lower curve is the estimated distribution from background events alone. The *np* elastic events with poor $\sum \chi^2 (\geq 15)$ are due primarily to low-energy neutrons in the beam.

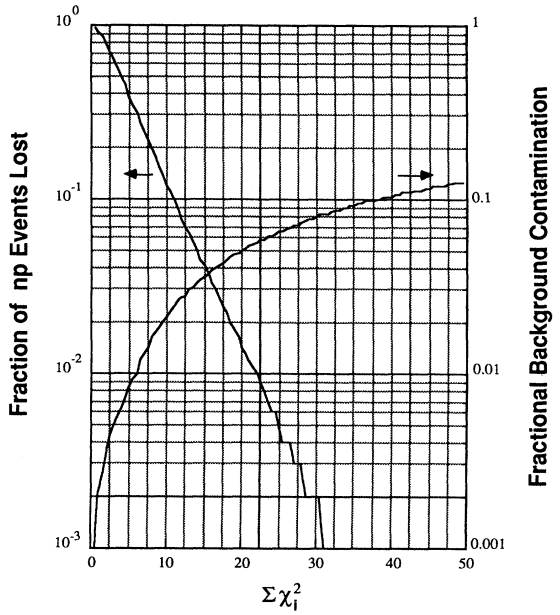

FIG. 12. The estimated fraction of lost *np* elastic-scattering events and the remaining fraction of background as a function of the $\Sigma\chi^2$ constraint. These estimates are based on the data shown in Fig. 11.

the shape of the "veto" events agrees well with the data from the graphite target. The background fraction was estimated using a polynomial fit to the data from the graphite target with the central region between $\pm 3°$ excluded. The number of inelastic events in the tails of the graphite data was normalized to the tails of the butanol data. The integrated background between the limits defined by the $\chi_i^2 < 5$ cut on the coplanarity was then calculated from the fit and found to be about 1.5%. Again, this procedure overestimates the background because multiple scattering can cause some *np* elastic events to have coplanarities in the tails of the distribution.

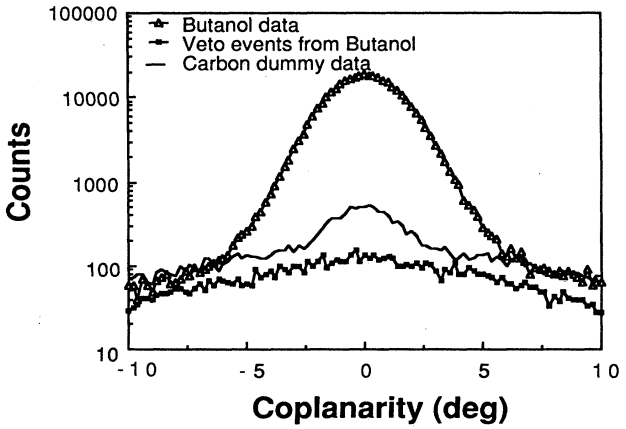

FIG. 13. The *np* coplanarity distribution for butanol target data is shown in the upper curve. The lower curve is obtained from the butanol-target data when the proton boom veto counter was triggered. These are necessarily inelastic-scattering events. The center curve is from the top half of the FST during the graphite-target run. A residual *np* elastic-scattering peak is seen. The butanol- and graphite-target data have been normalized in the tails of the distribution.

The most accurate estimates of the background fraction were obtained by scaling the background in the graphite target run to correct for the differences in the amount of nonhydrogenous material in the graphite target and the butanol-filled target, and to normalize the relative integrated neutron beam fluxes. Estimates were made separately for both holding field directions and for both left and right events from the graphite target data to check for any dependence on the angular acceptance of the left- and right-detection systems. The acceptances differed because the target magnetic holding field changed slightly when it was reversed because of the cyclotron fringe field. With the $\chi_i^2 < 5$ constraint it was found that the ratio of inelastic to total events from the top half of the graphite target was 0.30 ± 0.04. This ratio was averaged for left and right events and for the two magnetic holding field directions since no statistically significant dependence on these conditions was observed. By comparison, for the $\chi_i^2 < 9$ constraint, the ratio was larger, 0.52 ± 0.04.

The estimated contamination of inelastic events in the butanol target data for the $\chi^2 < 5$ constraint was found to be 0.010 ± 0.003. The good agreement between the three procedures shows that the background contributions were well understood. Estimates based on published quasielastic cross sections and a Monte Carlo simulation of the experiment also gave comparable results and the simulations of background events have $\Sigma\chi^2$ distributions very similar to that of the lower curve in Fig. 11(c).

The graphite target asymmetries were evaluated using the same $\chi_i^2 < \eta$ and $\Sigma\chi^2 < \xi$ conditions as for the butanol target data. There was no significant dependence on the conditions chosen and the background asymmetry was consistent with zero within the experimental accuracy. The correction for the background asymmetry was obtained from the $\chi_i^2 < 5$ data. The results are summarized in Table II.

Unlike the *np* elastic-scattering data, the (n,np) background asymmetries based on proton and neutron angles are not correlated. The background asymmetry at the elastic scattering zero-crossing angle was calculated for both the proton and neutron scattering angle distributions for several kinematic constraints. The overlap method of Eq. (10) was used.

Using the definition of $\Delta\theta$ and the fact that A_n (*np* elastic) in Eq. (14) is zero by choice at $\theta_{0p}(A_n)$, the corrected $\Delta\theta_p$ for *np* elastic scattering can be written

$$\Delta\theta_p(\text{true}) = \Delta\theta_p(\text{measured}) + \frac{r_b A_b}{(1-r_b) dA/d\theta} , \qquad (15)$$

where $\Delta\theta_p$ (measured) is the effect with the butanol-filled target, A_b is the measured analyzing power for the graphite target data at the zero-crossing angle, and r_b is the ratio of background to detected events satisfying all cuts applied to the *np* elastic-scattering data.

At the c.m. zero-crossing angle $\theta_0(A_n)$, which was

TABLE VI. Summary of the experimental $\Delta\theta_p$ and $\Delta\theta_n$ systematic errors. The error estimate is obtained from the sample standard deviation of all different tests for that item. The total is summed in quadrature.

Item	$\Delta\theta_p$	$\Delta\theta_n$
Fitting procedures	0.008°	0.009°
χ^2 constraints	0.019°	0.028°
Neutron scintillator bar discrimination threshold	0.025°	0.033°
Background subtraction	0.020°	0.020°
Independent analyses	0.045°	0.050°
Neutron scintillator bar TDC length		0.010°
Fluctuations in neutron scintillator bar timing		0.040°
TDC nonlinearities		0.060°
Total	0.058°	0.100°

determined to be 69.95°±0.20 (this value may have systematic errors associated with it), the proton-angle-based scattering asymmetry for the (n,np) background was found to be $\epsilon_b(\theta_{0p})=0.002\pm0.042$, and similarly, the neutron angle based background asymmetry was $\epsilon_b(\theta_{0n})=0.013\pm0.042$. The average proton-beam polarization during the background run was 0.66 ± 0.01, resulting in a neutron-beam polarization of 0.51 ± 0.01. The correction for background is summarized in Table II.

E. Summary of systematic errors

Possible systematic errors in the data and the off-line analyses have been investigated in detail, primarily by using a variety of cuts on the selected events. The conditions examined include: (i) the χ_i^2 constraint was varied between $\chi_i^2<4$, 5, 7.5, and 9; (ii) a $\sum\chi^2<10$, 15, or 20 was used in place of a χ_i^2 constraint; (iii) the cut on the neutron scintillator bar pulse-height distribution was varied between PHT>0, 15, 20, 25 channels; (iv) the number of neutron scintillator bars used in the data set was varied and the results from individual bars compared; (v) different angle ranges and calculation procedures were used in determining θ_0; (vi) two independent analyses of the data were made; and (vii) results derived from the neutron or proton scattering angles were obtained. Estimates of systematic uncertainty associated with background subtraction were also made in a similar fashion. It is emphasized that geometrical biases caused by the apparatus do not affect $\Delta\theta_p$ or $\Delta\theta_n$ because the effects cancel for the CSB difference $\theta_0(A_n)-\theta_0(A_p)$ provided that the biases do not change between the A_n and A_p parts of the experiment.

The systematic errors are summarized in Table VI. Although a systematic error entry for the background correction is included separately in the table, contributions from this source are also included implicitly in the tests associated with the χ^2 cuts since the background fraction changes by about a factor of 5 for the conditions chosen.

An additional effect due to uncertainty in the neutron scintillator bar length expressed in TDC units must be included in the calculation of the systematic error for $\Delta\theta_n$ since it scales proportionally. Timing drifts from run to run in the PMT's viewing the neutron scintillator bars also affected the determination of the neutron angles directly. These were typically ±0.05° in θ_n(lab) for any given bar. Corrections for the drifts were obtained from the button events, but this adds an additional statistical component to the error in $\Delta\theta_n$. Other known contributions affecting only θ_n were not studied in detail.

Systematic error estimates were determined by using the sample standard deviation for $\Delta\theta_p$ for the groups of individual conditions investigated. The total systematic error estimate is obtained by combining the individual conditions in quadrature. This is realistic because there is no evidence of systematic trends when the parameters are varied, and all fluctuations were of a statistical nature. "Theoretical" estimates of contributions to systematic errors in ΔA obtained from the observed beam and target properties, and geometrical imperfections are all much smaller than the statistical error.

Finally, as a check against errors in the analysis, two independent analyses were made for all but the final stages of extracting ΔA. They were compared for most of the conditions summarized in Tables I–IV. In general the differences between the two analyses were comparable to their internal fluctuations and there is no evidence for any significant discrepancy. The value summarized in Table VI is the sample standard deviation of all comparisons made and is only $\frac{1}{3}$ of the statistical error. This is considered to be very reasonable agreement considering the known differences in procedures and the resulting event samples.

IV. CONCLUSIONS

The experimental values of $\Delta\theta$ and $\Delta A=A_n-A_p$ at the analyzing power zero-crossing angle were determined from the observed values of θ_0:

$$\Delta\theta_p=\theta_{0p}(A_n)-\theta_{0p}(A_p)$$
$$=+0.340°\pm0.162°\pm(0.058°) \quad (16)$$

for the proton scattering angles and

$$\Delta\theta_n = \theta_{0n}(A_n) - \theta_{0n}(A_p) = +0.414° \pm 0.161° \pm (0.100°) \quad (17)$$

based on the neutron scattering angles. The first error quoted is the statistical uncertainty and the second is the estimate of systematic uncertainty. The appropriate corrections for background from (n,np) reactions have been applied.

The slope of the analyzing power at the zero-crossing angle is needed in the interpretation of this experiment. It was determined from a linear fit to various phase-shift predictions for a $\pm 1°$ region about the predicted crossover angle. The Saclay-Geneva analysis[34] gives $dA/d\theta = -0.01382$ deg^{-1} and a crossover angle of 69.44° while the Arndt *et al.*[29] phase-shift analysis (SP88) gives $dA/d\theta = -0.01254$ deg^{-1} and a crossover angle of 71.69°. Differences in the slope of the analyzing powers between the two phase-shift analyses are large compared to their estimated statistical uncertainty and the effect on ΔA is not negligible ($\frac{1}{3}\sigma$) compared to the error in the present experiment. It appears that there are inconsistencies in the analyzing power data base between 400 and 500 MeV and the selections of data in the two phase-shift analyses are probably not equivalent.[35]

Preliminary results[36] of new measurements at TRIUMF at 425 MeV indicate that the Saclay-Geneva phase-shift analysis gives a slightly better prediction for the analyzing power. This is also confirmed by the better agreement between the observed zero-crossing angle and that prediction. The observed slopes for ϵ_p and ϵ_n were -0.0105 ± 0.0002 deg^{-1} and -0.0069 ± 0.0002 deg^{-1}, respectively. The derived values of $dA/d\theta$ are -0.0136 deg^{-1} and -0.0135 deg^{-1}. These also favor the Saclay-Geneva solution. Therefore the Saclay-Geneva value was used to obtain the final results for ΔA which are found in Table II. Note however, that at 188 MeV, the energy of the on-going Indiana University Cyclotron Facility (IUCF) experiment,[37] the Saclay-Geneva predictions do not appear to give a reasonable value of the zero-crossing angle. No systematic error is included in the interpretation of the present result for the phase-shift uncertainties since changes in the slope of the analyzing power can easily be incorporated in the future and it is preferable to separate errors of a random nature from such subjective uncertainties.

Using the Saclay-Geneva value, $dA/d\theta = -0.01382$ deg^{-1}, the difference between A_n and A_p at θ_0 is

$$\Delta A(\theta_p) = +0.0047 \pm 0.0022(\pm 0.0008)\,, \quad (18)$$

based on the laboratory proton scattering angles, and

$$\Delta A(\theta_n) = +0.0057 \pm 0.0022(\pm 0.0013)\,, \quad (19)$$

based on laboratory neutron scattering angles. A scale error of about 10% for the present uncertainties in the phase-shift solutions is appropriate. This should diminish considerably in the next iteration of fitting. The result derived from the proton scattering angles is preferred because the additional systematic errors associated with the neutron scattering angles could not all be evaluated in detail.

The preliminary result of the present experiment has stimulated several calculations of ΔA. The calculation of Williams, Thomas, and Miller[17] (WTM) is summarized in Table VII. Their calculation used the Reid soft-core potential to evaluate contributions from one photon exchange, the neutron-proton mass difference (Δm) in one pion and ρ exchanges, and ρ-ω meson mixing. They obtained $\Delta A = 50 \times 10^{-4}$ at 477 MeV near the analyzing power zero-crossing angle. At the zero-crossing angle, ΔA is dominated by the contribution of Δm in one-pion exchange while the one-photon-exchange term is small. The ρ-ω term is also small, which is unfortunate. Iqbal and Niskanen[38] have also included the effects of the σ, ω, and A_1 mesons and find all the contributions to be small.

A similar calculation by Ge and Svenne[18] (GS) using the Paris potential yielded $\Delta A = 74 \times 10^{-4}$. This calculation did not include the effect of Δm in ρ exchange and there were deficiencies in the calculation of the one-photon-exchange term. The effect of Δm in one-boson exchange has also been investigated by Holzenkamp, Holinde, and Thomas[19] (HHT) using a momentum-space version of the Bonn potential. Taking the one photon exchange and ρ-ω-mixing terms from WTM, the HHT result with an "exact" calculation for one boson exchanges is $\Delta A = 47 \times 10^{-4}$ at the zero-crossing angle. The three "conventional" calculations are in reasonable agreement although one can identify differences in the details that account for the small variations in the sizes of the individual terms. This agreement suggests that model dependence of the strong distorting waves is negligible for models based on one-boson exchange. There is one exception to this: Beyer and Williams[39] have shown that the coordinate-space Bonn potential prediction does not agree with the present experiment. Since the primary difference in the models is the short-range behavior, there would appear to be some deficiency at short range in the coordinate-space representation of the Bonn potential. Beyer and Williams also show that the Virginia-Mainz hybrid quark-meson potential yields reasonable predictions. The contributions of the dominant CSB mechanisms in a system of six valence quarks appears to be negligible.[17,20] The angular dependence of the WTM pre-

TABLE VII. Calculations by Williams, Thomas, and Miller (Ref. 17) of $10^4 \Delta A$ as a function of laboratory energy to show the relative importance of various contributions at the analyzing-power zero-crossing angle.

Energy	477 MeV	350 MeV	188 MeV
θ_0 (c.m.)	70°	72°	96°
1γ exchange	5.	3.	8.
1π exchange	43.	42.	7.
2π exchange	−0.4	0.1	−0.5
ρ exchange	8	6	1
ρ-ω mixing	−6	−3	5
Total	50	48	17
Experiment	47±22(±8)		

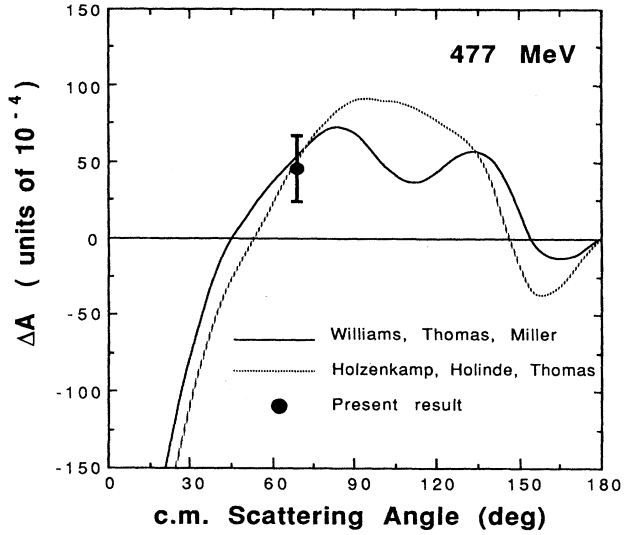

FIG. 14. The analyzing-power differences $\Delta A(\theta) = A_n(\theta) - A_p(\theta)$ for *np* elastic scattering at 477 MeV from Williams, Thomas, and Miller (Ref. 17) and Holzenkamp, Holinde, and Thomas (Ref. 19) are shown with the result of the present measurement.

dictions are compared with the experimental result at 477 MeV in Fig. 14.

Iqbal, Thaler, and Woloshyn[21] (ITW) have used a purely relativistic approach starting from the Bethe-Salpeter equation and a covariant representation of the *NN* on-shell scattering matrix and get $\Delta A = 11 \times 10^{-4}$. Much of the disagreement with the other predictions has been attributed to the soft value used for the pion form factor, which causes the dominant CSB contribution from one-pion exchange to be suppressed.[38–40] This has been demonstrated in both the calculation of Ref. 38 and by Iqbal[40] where it is emphasized that a reliable model for the form factors is needed. There is also ambiguity in the prescription used for the off-shell extrapolation of the *T*-matrix in the relativistic approach. It can be shown that the conventional and relativistic treatments are formally equivalent.[15]

The experimental result is the first measurement of a class (IV) charge-symmetry-breaking effect in the free *NN* interaction. It is in reasonably good agreement with theory, but possibly excludes one version of modern potential models. The value observed confirms the extension of the conventional one-boson-exchange potentials to the previously unmeasured class (IV) *NN* interaction. Work is currently underway to measure the CSB parameter $\Delta A = A_n - A_p$ at lower incident neutron-beam energies, 350 MeV at TRIUMF (Ref. 41) and 188 MeV at IUCF (Ref. 37). Additional precise measurements are required to extract information regarding the individual terms contributing to the charge-symmetry-breaking interaction. The ρ-ω term is of particular interest, since it relates directly to the one-boson-exchange description of the *NN* interaction at short distances.

ACKNOWLEDGMENTS

The authors would like to acknowledge useful discussions with H. E. Conzett and F. Lehar. The extraordinary efforts of the TRIUMF ion source group in producing record polarized beam currents for this experiment are greatly appreciated. This work was supported in part by the Natural Sciences and Engineering Research Council of Canada.

*Present address: Pharma Department, Sandoz A.G., CH-4002, Basel, Switzerland.
†Present address: Saskatoon Cancer Clinic, Saskatoon, Saskatchewan S7K 6Z2.
‡Present address: Jet Propulsion Laboratory, Pasadena, California 91109.
§Present address: Science World, Vancouver, British Columbia V6B 5E7.
**Present address: Department of Physics, University of Victoria, Victoria, British Columbia V8W 2Y2.
††Present address: MacDonald-Detweiler, Vancouver, British Columbia.
‡‡Present address: Institute for High Energy Physics, Academia Sinica, P.O. Box 918, Beijing, China.

[1]W. Heisenberg, Z. Phys. **77**, 1 (1932).
[2]O. Dumbrajs, R. Koch, H. Pilkuhn, G. C. Oades, H. Behrens, J. J. de Swart, and P. Kroll, Nucl. Phys. **B216**, 277 (1983).
[3]J. A. Nolen and J. P. Schiffer, Annu. Rev. Nucl. Sci. **19**, 471 (1969).
[4]S. Shlomo, Rep. Prog. Phys. **41**, 937 (1978).
[5]S. A. Coon and R. C. Barrett, Phys. Rev. C **36**, 2189 (1987).
[6]B. Gabioud, J-C. Alder, C. Joseph, J-F. Loude, N. Morel, A. Perrenoud, J. P. Perroud, M. T. Tran, E. Winkelmann, W. Dahme, E. Panke, D. Renker, G. Strassner, P. Truöl, and G. F. de Teramond, Nucl. Phys. **A420**, 496 (1984).
[7]O. Schori, B. Gabioud, C. Joseph, J. P. Perroud, D. Rüegger, M. T. Tran, P. Truöl, E. Winkelmann, and W. Dahme, Phys. Rev. C **35**, 2252 (1987).
[8]E. Pedroni, K. Gabathuler, J. J. Domingo, W. Hirt, P. Schwaller, J. Arvieux, C. H. Q. Ingram, P. Gretillat, J. Piffaretti, N. W. Tanner, and C. Wilkin, Nucl. Phys. **A300**, 321 (1978).
[9]T. G. Masterson, J. J. Kraushaar, R. J. Peterson, R. S. Raymond, R. A. Ristinen, J. L. Ullman, R. L. Boudrie, D. R. Gill, E. F. Gibson, and A. W. Thomas, Phys. Rev. C **30**, 2010 (1984).
[10]T. G. Masterson, J. J. Kraushaar, R. J. Peterson, R. S. Raymond, R. A. Ristinen, R. L. Boudrie, E. F. Gibson, and A. W. Thomas, Phys. Rev. C **26**, 2091 (1982).
[11]G. R. Smith, D. R. Gill, D. Ottewell, G. D. Wait, P. Walden, R. R. Johnson, R. Olszewski, R. Rui, M. E. Sevior, R. P. Trelle, J. Brack, J. J. Kraushaar, R. A. Ristinen, H. Chase, E. L. Mathie, V. Pafilis, R. B. Shubank, N. R. Stevenson, A. Rinat, and Y. Alexander, Phys. Rev. C **38**, 240 (1988).
[12]E. M. Henley and G. A. Miller, in *Mesons in Nuclei*, edited by M. Rho and D. Wilkinson (North-Holland, Amsterdam, 1979), Vol. I, p. 416.
[13]J. Bystricky, F. Lehar, and P. Winternitz, J. Phys. (Paris) **39**, 1 (1978).

[14]A. Gersten, Phys. Rev. C **24**, 2174 (1981).
[15]A. Gersten, L. G. Greeniaus, J. A. Niskanen, S. Ishikawa, T. Sasakawa, and A. W. Thomas, Few Body Systems **3**, 171 (1988).
[16]G. A. Miller, A. W. Thomas, and A. G. Williams, Phys. Rev. Lett. **56**, 2567 (1986).
[17]A. G. Williams, A. W. Thomas, and G. A. Miller, Phys. Rev. C **34**, 756 (1987).
[18]L. Ge and J. P. Svenne, Phys. Rev. C **33**, 417 (1986); **34**, 756 (E) (1986).
[19]B. H. Holzenkamp, K. Holinde, and A. W. Thomas, Phys. Lett. B **195**, 121 (1987).
[20]K. Brauer, E. M. Henley, and G. A. Miller, Phys. Rev. C **34**, 1779 (1986).
[21]J. Iqbal, J. Thaler, and R. Woloshyn, Phys. Rev. C **36**, 2442 (1987).
[22]R. Abegg, J. Birchall, E. B. Cairns, G. H. Coombes, C. A. Davis, N. E. Davison, P. P. J. Delheij, P. W. Green, L. G. Greeniaus, H. P. Gubler, D. C. Healey, C. Lapointe, W. P. Lee, W. J. McDonald, C. A. Miller, G. A. Moss, G. R. Plattner, P. R. Poffenberger, W. D. Ramsay, G. Roy, J. Soukup, J. P. Svenne, R. R. Tkachuk, W. T. H. van Oers, G. D. Wait, and Y. P. Zhang, Nucl. Instrum. Methods **A234**, 11 (1985).
[23]R. Abegg, J. Birchall, E. B. Cairns, G. H. Coombes, C. A. Davis, N. E. Davison, P. P. J. Delheij, P. W. Green, L. G. Greeniaus, H. P. Gubler, D. C. Healey, C. Lapointe, W. P. Lee, W. J. McDonald, C. A. Miller, G. A. Moss, G. R. Plattner, P. R. Poffenberger, W. D. Ramsay, G. Roy, J. Soukup, J. P. Svenne, R. R. Tkachuk, W. T. H. van Oers, G. D. Wait, and Y. P. Zhang, Nucl. Instrum. Methods **A234**, 20 (1985).
[24]R. Abegg, D. Bandyopadhyay, J. Birchall, E. B. Cairns, G. H. Coombes, C. A. Davis, N. E. Davison, P. P. J. Delheij, P. W. Green, L. G. Greeniaus, H. P. Gubler, D. C. Healey, C. Lapointe, W. P. Lee, W. J. McDonald, C. A. Miller, G. A. Moss, G. R. Plattner, P. R. Poffenberger, W. D. Ramsay, G. Roy, J. Soukup, J. P. Svenne, R. R. Tkachuk, W. T. H. van oers, G. D. Wait, and Y. P. Zhang, Nucl. Instrum. Methods **A254**, 469 (1987).
[25]P. P. J. Delheij, D. C. Healey, and G. D. Wait, Nucl. Instrum. Methods **A264**, 186 (1988).
[26]P. P. J. Delheij, D. C. Healey, and G. D. Wait, *Proceedings of the 6th International Symposium on Polarization Phenomena in Nuclear Physics,* 1985, edited by M. Kondo *et al.* [J. Phys. Soc. Jpn. Suppl. **55**, 1090 (1986)].
[27]R. Abegg, D. Bandyopadhyay, J. Birchall, E. B. Cairns, G. H. Coombes, C. A. Davis, N. E. Davison, P. P. J. Delheij, P. W. Green, L. G. Greeniaus, H. P. Gubler, D. C. Healey, C. Lapointe, W. P. Lee, W. J. McDonald, C. A. Miller, G. A. Moss, G. R. Plattner, P. R. Poffenberger, W. D. Ramsay, G. Roy, J. Soukup, J. P. Svenne, R. R. Tkachuk, W. T. H. van Oers, G. D. Wait, and Y. P. Zhang, Phys. Rev. Lett. **56**, 2571 (1986).
[28]R. R. Tkachuk, Ph.D. thesis, University of Alberta, 1987.
[29]Interactive Dial-In-Program, SAID, by R. A. Arndt. Predictions were taken from the single energy fit C500, Spring, 1988, and the February 1987 Saclay-Geneva solution.
[30]T. S. Bhatia, G. Glass, J. C. Hiebert, L. C. Northcliffe, W. B. Tibbens, B. E. Bonner, J. E. Simmons, C. L. Hollas, C. R. Newsom, P. J. Riley, and R. D. Ransome, Phys. Rev. C **24**, 796 (1981).
[31]L. G. Greeniaus and J. Soukup, TRIUMF Report No. TRI-DNA-81-1, 1981 (unpublished).
[32]D. V. Bugg and C. Wilkin, Nucl. Phys. **A467**, 575 (1987).
[33]G. E. Edwards and D. A. Hutcheon (private communication).
[34]F. Lehar, C. Lechanoine-Leluc, and J. Bystricky, J. Phys. (Paris) **48**, 199 (1987); (private communication).
[35]F. Lehar (private communication).
[36]R. Abegg, D. Bandyopadhyay, J. Birchall, C. A. Davis, N. E. Davison, P. P. J. Delheij, P. W. Green, L. G. Greeniaus, D. C. Healey, C. Lapointe, W. J. McDonald, C. A. Miller, G. A. Moss, S. A. Page, W. D. Ramsay, N. Rodning, G. Roy, W. T. H. van Oers, G. D. Wait, and J. Watson, Bull. Am. Phys. Soc. **32**, 1546 (1987).
[37]S. E. Vigdor, in *Current Problems in Nuclear Physics,* edited by T. Paredellis and S. Kassionides (Hellenic Physical Society, Athens, Greece, 1986), p. 193.
[38]M. J. Iqbal and J. A. Niskanen, Phys. C **38**, 2259 (1988).
[39]M. Beyer and A. G. Williams, Phys. Rev. C **38**, 779 (1988).
[40]M. J. Iqbal (private communication).
[41]R. R. Tkachuk, L. G. Greeniaus, and W. T. H. van Oers, TRIUMF Experiment No. 369 proposal (unpublished).